Modeling and identification

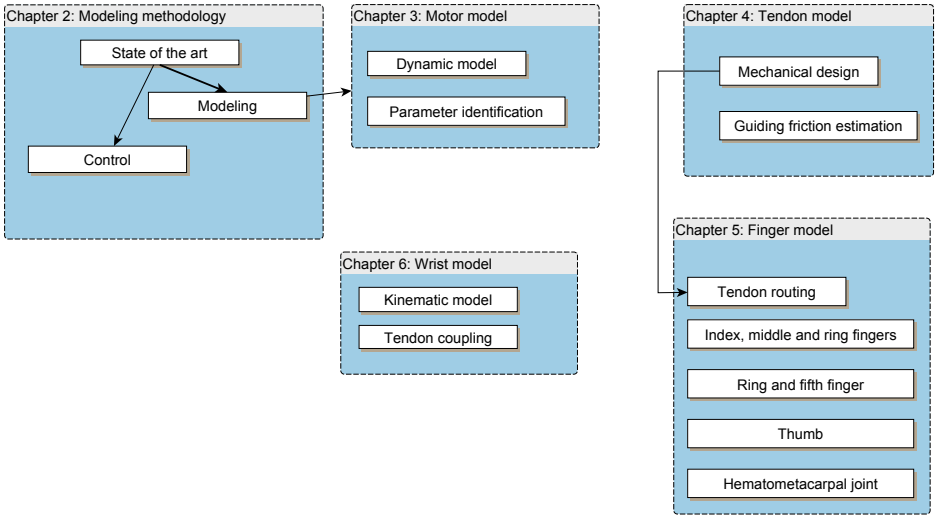

Figure 1.17: Overview of the structure of the modeling part

In this part, the mechanical modeling of the hand is conducted. The modeling starts with the motors and is progressively extended to the fingers. The nonlinear spring mechanisms and the tendons are modeled. Experiments are performed step by step to verify the models. modeling. The logical links between the different chapters of this part are depicted in Fig. 1.17.

In the first chapter, the general methodology is presented. Dynamics modeling methods such as the Lagrangian and the Newton-Euler methods are introduced and are later used to establish the dynamic model for the fingers. The second chapter details the modeling of the motors. A precise modeling of the friction and a set of friction compensation methods is proposed. Experimental results are reported that confirm the benefits of the compensations.

The third chapter concentrates on the modeling of the tendon behavior. A complete characterization of several tendon types and materials is performed. A tendon model is established such that the mechanical designer has the tools to decide between the use of pullies guidings or sliding surfaces.

The fourth chapter presents the kinematic modeling of the fingers. However, because each finger has a slightly different design (e. g. the thumb tensegrity structure or the underactuated joints), the specificities of each finger are detailed in separate chapters. The couplings between the motor motion and the finger motion are derived and the pseudo inverse matrix is used to estimate the link side position from the tendon displacements. A dynamic model of the index finger is presented and several simulations are performed to derive a simplified dynamic model.

Finally, the wrist kinematic modeling is reported in the fifth chapter. The influence of the wrist motion on the tendon displacement is analyzed. Simulations and experiments are performed to show that the kinematic model can be successfully used to compensate the wrist coupling.

2 Modeling approaches

This chapter reports the different methods used to create the kinematic models and the dynamic models of the fingers. In the first section, the generic symbols and units used in the thesis are reported. The second section presents the kinematic modeling. The third section presents two well known dynamic modeling methods. Finally, a short discussion summarizes the chapter.

2.1 Symbols and units

The units used through the thesis comply with the international units and are reported in table 2.1.

2.2 Kinematic modeling approaches

Robotic manipulators represent a subclass of mechanisms that have a specific mechanical structure. Most often, they consist of a serial connection of links connected by revolute or prismatic joints. Although other types of joint exist, the use of electromotors for the actuation and ball bearings for the guidings leads to those two principal types. The transformation of the robot end-effector is obtained by cumulating the transformation of each link in the chain, starting from the base. Homogeneous transformation matrices are used to establish kinematic models. It circumvents the ambiguity of the Denavit-Hartenberg [99] notation while having negligible impact on the real-time system. Indeed, the implementation is performed through the use of formal manipulation softwares (Maple^{TM}) and C language export.

2.3 Dynamic modeling approaches

Dynamic modeling approaches are used to established the dynamic equations of motion in the form

$$\boldsymbol{M}(\boldsymbol{q})\ddot{\boldsymbol{q}} + \boldsymbol{C}(\boldsymbol{q}, \dot{\boldsymbol{q}})\dot{\boldsymbol{q}} + \boldsymbol{g}(\boldsymbol{q}) = \boldsymbol{\tau}, \tag{2.1}$$

where $n \in \mathbb{N}$ is the number of links, $\boldsymbol{M}(\boldsymbol{q}) \in \mathbb{R}^{n\times n}$, $\boldsymbol{C}(\boldsymbol{q}, \dot{\boldsymbol{q}}) \in \mathbb{R}^{n\times n}$, $\boldsymbol{g}(\boldsymbol{q}) \in \mathbb{R}^n$ are respectively the inertia matrix, the Coriolis and centrifugal effects and the gravity torque covector. $\boldsymbol{q} \in \mathbb{R}^n$ and $\boldsymbol{\tau} \in \mathbb{R}^n$ are the joint position and the motor torque vector.

A dynamic model of the system is paramount for any analysis and controller design. Numerous techniques have been developed to establish the system of second order differential equations, such as Lagrange-Euler, recursive Lagrangian and Newton-Euler methods. Each approach leads to the

Description	Unit	Symbol
Time	seconds	[s]
Length	meters	[m]
Mass	kilograms	[kg]
Angle	radians	[rad]
Torque	Newton meter	[Nm]
Force	Newton	[N]
Linear velocity	meters per second	[m/s]
Angular velocity	radians per second	[rad/s]
Linear acceleration	meters per second squared	[m/s^2]
Angular acceleration	radians per second squared	[rad/s^2]
Linear stiffness	Newton per meter	[N/m]
Angular stiffness	Newton meter per radian	[Nm/rad]

Table 2.1: Symbols and units

same behavior [100], but the computation burdens are different. One can refer to [101] for a comparison of the different methods applied on different types of robot.

2.3.1 Newton-Euler approach

The Newton-Euler method is a recursive method based on the equilibrium of forces and torques. In numerous papers and text books, the method is used to establish the dynamic equations. The equations reported here are based on Craig [102]. Several software packages such as Symoro+ [103] have been developed based on this algorithm, in order to simplify the modeling process. More recently, in [104] De Luca proposed to modify the genuine method in order to reduce the computational effort to obtain the Coriolis/centrifugal and inertia matrices.

The Newton-Euler method proceeds in two phases: first the velocity and acceleration are computed from base to end-effector. Then, the forces and torques are computed from end-effector to base.

Base equations

A free body of mass $m \in \mathbb{R}^+$ subject to a force $\boldsymbol{F} \in \mathbb{R}$ acting on the center of mass results in an acceleration $\boldsymbol{a} \in \mathbb{R}$ according to Newton's law

$$\boldsymbol{F} = m\boldsymbol{a}. \tag{2.2}$$

Similarily for the torque, Euler's equation gives

$$\boldsymbol{N} = \boldsymbol{I}\dot{\boldsymbol{\omega}} + \boldsymbol{\omega} \times \boldsymbol{I}\boldsymbol{\omega}, \tag{2.3}$$

where $\boldsymbol{N} \in \mathbb{R}$ is the body torque. $\boldsymbol{I} \in \mathbb{R}$ and $\boldsymbol{\omega} \in \mathbb{R}$ are the link inertia expressed at the center of mass and the angular velocity.

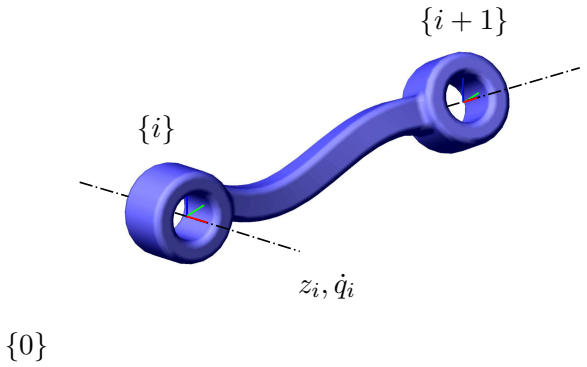

Figure 2.1: Isolated link i

Forward equations

The position, velocity and acceleration of all links are propagated from bottom to end-effector. Considering a chain of $n \in \mathbb{N}$ bodies connected with n revolute joints. Starting from the base link $< 0 >$ attached to frame $\{0\}$ (cf. Fig. 2.1) up to the end effector link $< n >$ attached to frame $\{n\}$. The velocities and accelerations of the link are obtained from the previous link with

$$ {}^{i+1}\boldsymbol{v}_{i+1} = {}^{i+1}_{i}\mathbf{R}[{}^{i}\boldsymbol{v}_i + ({}^{i}\boldsymbol{\omega}_i \times {}^{i}\boldsymbol{p}_{i+1,i})], \tag{2.4} $$

and

$$ {}^{i+1}\boldsymbol{a}_{i+1} = {}^{i+1}_{i}\mathbf{R}[{}^{i}\dot{\boldsymbol{\omega}}_i \times {}^{i}\boldsymbol{p}_{i+1,i} + {}^{i}\boldsymbol{\omega}_i \times ({}^{i}\boldsymbol{\omega}_i \times {}^{i}\boldsymbol{p}_{i+1,i}) + {}^{i}\boldsymbol{a}_i], \tag{2.5} $$

where $\forall i \in [0 \dots n-1]$, ${}^{i}\boldsymbol{v}_i \in \mathbb{R}^3$ is the linear velocity of link i with respect to the frame $\{0\}$ expressed in $\{i\}$. ${}^{i}\boldsymbol{\omega}_i \in \mathbb{R}^3$ is the the angular velocity of link i with respect to $\{0\}$ expressed in $\{i\}$, ${}^{i}\boldsymbol{p}_{i+1,i} \in \mathbb{R}^3$ is the vector between the rotation center of body $< i >$ and body $< i+1 >$ rotation points, expressed in $\{i\}$.

Similarily, ${}^{i}\boldsymbol{a}_i \in \mathbb{R}^3$ is the linear acceleration of link i with respect to $\{0\}$ expressed in $\{i\}$ and ${}^{i}\dot{\boldsymbol{\omega}}_i \in \mathbb{R}^3$ is the angular acceleration of the link i expressed in $\{i\}$.

The angular velocities in world coordinates are transformed with

$$ {}^{0}\boldsymbol{\omega}_{i+1} = {}^{0}\boldsymbol{\omega}_i + \dot{q}_{i+1}{}^{0}\boldsymbol{z}_{i+1} \tag{2.6} $$

In the previous link coordinates,

$$ {}^{i+1}\boldsymbol{\omega}_{i+1} = {}^{i+1}_{i}\mathbf{R}{}^{i}\boldsymbol{\omega}_i + \dot{q}_{i+1}{}^{i+1}\boldsymbol{z}_{i+1}, \tag{2.7} $$

$\forall i \in [1 \dots n]$, ${}^{0}\boldsymbol{\omega}_i \in \mathbb{R}^3$(resp. ${}^{i}\boldsymbol{\omega}_i \in \mathbb{R}^3$), denotes the angular velocity of link i with respect to $\{0\}$ (resp. $\{i\}$), ${}^{0}\boldsymbol{z}_{i+1} \in \mathbb{R}^3$ (resp. ${}^{i+1}\boldsymbol{z}_{i+1} \in \mathbb{R}^3$) is the rotation axis expressed in $\{0\}$ (resp. $\{i+1\}$) and $\dot{q}_{i+1} \in \mathbb{R}$ is the rotational velocity of link $i+1$ with respect to the link i (i. e. the joint velocity).

The angular accelerations are:

$$^{i+1}\dot{\boldsymbol{\omega}}_{i+1} = {}^{i+1}_{i}\mathbf{R}\,{}^{i}\dot{\boldsymbol{\omega}}_{i} + {}^{i+1}_{i}\mathbf{R}\,{}^{i}\boldsymbol{\omega}_{i} \times \dot{q}_{i+1}\,{}^{i+1}\boldsymbol{z}_{i+1} + \ddot{q}_{i+1}\,{}^{i+1}\boldsymbol{z}_{i+1}, \tag{2.8}$$

where $\ddot{q}_i \in \mathbb{R}$ is the rotational acceleration of link $i+1$ with respect to link i (i. e. the joint acceleration).

In order to apply Newton's law, all linear accelerations must be expressed at the center of mass of each link. Recalling,

$$^{i}\boldsymbol{v}_{c,i} = {}^{i}\boldsymbol{v}_{i} + {}^{i}\boldsymbol{\omega}_{i} \times {}^{i}\boldsymbol{p}_{c,i}, \tag{2.9}$$

where $\forall i \in [1 \dots n]$, ${}^{0}\boldsymbol{p}_{c,i} \in \mathbb{R}^3$ is the vector from the origin to the center of mass of the link, expressed in $\{0\}$ and $\boldsymbol{v}_{c,i} \in \mathbb{R}^3$ is the linear velocity of the center of mass of the link i.

$$^{i}\boldsymbol{a}_{c,i} = {}^{i}\boldsymbol{a}_{i} + {}^{i}\dot{\boldsymbol{\omega}}_{i} \times {}^{i}\boldsymbol{p}_{c,i} + {}^{i}\boldsymbol{\omega}_{i} \times {}^{i}\boldsymbol{\omega}_{i} \times {}^{i}\boldsymbol{p}_{c,i}, \tag{2.10}$$

where $\forall i \in [1 \dots n]$, $\boldsymbol{a}_{c,i} \in \mathbb{R}^3$ is the linear acceleration of the center of mass of the link i.

At the end of the forward procedure, all velocities and accelerations of the center of mass of the links are expressed recursively with respect to the previous link. The laws of Euler and Newton yield

$$^{i+1}\boldsymbol{F}_{i+1} = m^{i+1}_{i+1}\boldsymbol{a}_{c,i+1} \tag{2.11}$$

$$^{i+1}\boldsymbol{N}_{i+1} = \boldsymbol{I}_{i+1}\,{}^{i+1}\dot{\boldsymbol{\omega}}_{i+1} + {}^{i+1}\boldsymbol{\omega}_{i+1} \times \boldsymbol{I}_{i+1}\,{}^{i+1}\boldsymbol{\omega}_{i+1} \tag{2.12}$$

where all inertia matrices $\boldsymbol{I}_i \in \mathbb{R}^{3\times3}, \forall i \in [1 \dots n]$ are expressed at the center of mass of the links.

Backward equations

In the backward phase, the forward equations are substituted in the Newton law of equilibrium in order to express the link's angular and linear accelerations depending on the joint torques and the gravity field. Expressing the force and torque balance yields

$$^{i}\boldsymbol{f}_{i} = {}_{i+1}^{i}\mathbf{R}\,{}^{i+1}\boldsymbol{f}_{i+1} + {}^{i}\boldsymbol{F}_{i}, \tag{2.13}$$

where $\boldsymbol{f}_i \in \mathbb{R}, i \in [1 \dots n]$ is the force exerted on link i by link $i-1$. Similarily the torque balance gives

$$^{i}\boldsymbol{\eta}_{i} = {}^{i}\boldsymbol{N}_{i} + {}_{i+1}^{i}\mathbf{R}\,{}^{i+1}\boldsymbol{\eta}_{i+1} + {}^{i}\boldsymbol{p}_{c,i} \times {}^{i}\boldsymbol{F}_{i} + {}^{i}\boldsymbol{p}_{i+1} \times {}_{i+1}^{i}\mathbf{R}\,{}^{i+1}\boldsymbol{f}_{i+1}, \tag{2.14}$$

where $\boldsymbol{\eta}_i \in \mathbb{R}, i \in [1 \dots n]$ is the torque exerted on link i by link $i-1$.

Finally, the joint torques are obtained as

$$\boldsymbol{\tau}_{i} = {}^{i}\boldsymbol{\eta}_{i}^{T\,i}\boldsymbol{z}_{i}. \tag{2.15}$$

2.3.2 Lagrange approach

The Lagrange method is based upon the fact that the change of energy of the system is equal to the power exchange with the environment. More formally, by introducing $\mathcal{L} = E_v - E_c$ the difference between the kinetic energy E_v and the potential energy E_c(elastic or gravity), and in the absence of frictional losses (also called the Rayleigh dissipation terms), the joint torques τ_i are directly obtained as:

$$\frac{d}{dt}\left(\frac{\partial \mathcal{L}}{\partial \dot{q}_i}\right) - \frac{\partial \mathcal{L}}{\partial q_i} = \tau_i, \quad \forall i \in [1 \dots n] \tag{2.16}$$

for a system with n degrees of freedom, where $\boldsymbol{q}$ is the state variable and $\mathcal{L}$ is the Lagragian of the system. Collecting the terms allows to write the dynamic equation as

$$\boldsymbol{M}(\boldsymbol{q})\ddot{\boldsymbol{q}} + \boldsymbol{C}(\boldsymbol{q}, \dot{\boldsymbol{q}})\dot{\boldsymbol{q}} + \boldsymbol{g}(\boldsymbol{q}) = \boldsymbol{\tau}_{ext}, \tag{2.17}$$

where $\boldsymbol{q} \in \mathbb{R}^n$ is the state vector, $\boldsymbol{M}(\boldsymbol{q}) \in \mathbb{R}^{n \times n}$ is the inertia matrix and $\boldsymbol{C}(\boldsymbol{q}, \dot{\boldsymbol{q}}) \in \mathbb{R}^n$ is the matrix of Coriolis and centrifugal terms. $\boldsymbol{g}(\boldsymbol{q}) \in \mathbb{R}^n$ is the covector of the gravity torques and $\boldsymbol{\tau}_{ext} \in \mathbb{R}^n$ is the covector of externally applied torques.

Deriving the dynamics equations with the Lagragian method mainly consists of expressing the Lagrangian $\mathcal{L}$ of the mechanical system and symbolically deriving the expressions for the torques $\tau_i, i \in [1 \dots n]$. The method can be applied to any not non-holonomic mechanism structure. It is a systematic method and can be applied programatically. However, applied without further considerations, the method generates computationally more expensive forms.

2.4 Discussion

The most important conclusion is, that, on the one hand the Lagrange-Euler method (very structured) leads to computationally expensive formulations. On the other hand the Newton-Euler methodology leads to more efficient computation forms (but is not well structured). Indeed, it is reported in [102] that the Lagrangian approach has a $O(n^3)$ complexity while the recursive Euler-Newton method is of complexity $O(n)$. Nonetheless, it should be noted that once the closed form equations are obtained, simplifications (factorization or code optimization) can lead to more efficient implementations. In this thesis, the Lagragian approach is selected, since, by observing the closed form structure, more insight into the possible control scheme is gained.

3 Motor model

Motors are the foundation layer of robotic systems. Highly dynamic motors are allowing to have high fast and precise positioning. This section models the motors used in the forearm to pull the tendons. The aim is to obtain a reliable dynamic motor model, and if possible to improve the motor behavior through the use of friction compensation or ripple (periodic disturbances) compensation mechanisms. Friction modeling and compensation techniques are presented in [57, 105–109]. The motors used have been designed and manufactured by a spin-off company of the Institute of Robotics and Mechatronics [110]. Figure 3.1 shows the motor, the power electronics, and the communication module. The motors are classified as PMSM (permanent magnet synchronous motors). The current control loop is executed in the communication electronics FPGA (Fast Programmable Gate Array: Xilinx Spartan 3e XCS500EP132) at 100kHz. All motor modules are connected to a data collector board via a BiSS (Bidirectional Synchronous Serial interface [111]). The data collector board features two FPGAs (V5LX50) and communicates with the real-time computer via an optical SpaceWire connexion (space qualified ESA standard [112]).

3.1 Dynamic model

The motors are modeled as a second order system with a velocity and position dependent friction (cf. Fig. 3.2). The total inertia expressed in the output shaft velocity is obtained from the fixed gear ratio α_{gear} (neglecting the harmonic drive elasticity) between input shaft and output shaft by considering the energy mapping.

$$B = B_{motor}\alpha_{gear}^{-2} + B_{gearbox}, \tag{3.1}$$

where $B \in \mathbb{R}$ is the total motor inertia seen at the output shaft. $B_{motor} \in \mathbb{R}$ is the motor shaft inertia alone. $B_{gearbox} \in \mathbb{R}$ is the inertia of the output

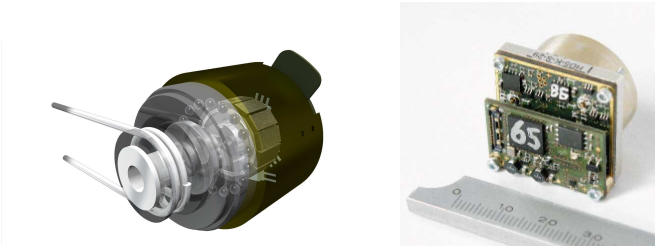

(a) Render (b) Photograph

Figure 3.1: Rendered motor module and real motor module

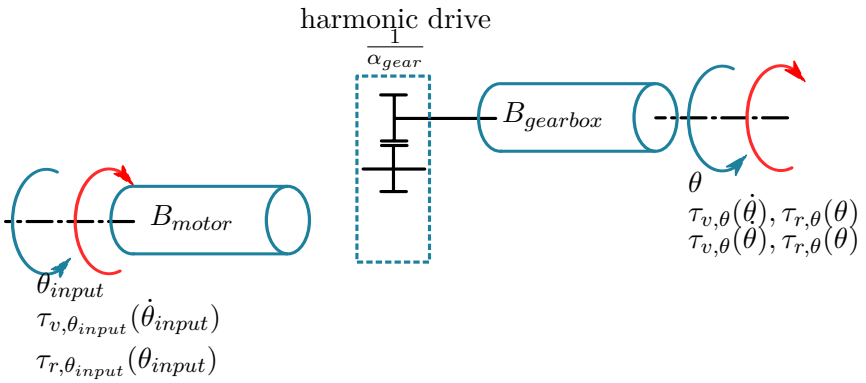

Figure 3.2: Model of the Permanent Magnet Synchronous Motors (PMSM) with a harmonic drive. The friction terms before and after the gear box are separated.

Table 3.1: Different contributions to the total motor friction

Description	Symbol
$\tau_{\mathrm{v}}(\dot{\theta}_{\mathrm{input}}) \in \mathbb{R}$	Velocity dependent friction due to the input shaft
$\tau_{\mathrm{v}}(\dot{\theta}) \in \mathbb{R}$	Velocity dependent friction due to the output shaft
$\tau_{\mathrm{r,input}}(\theta_{\mathrm{input}}) \in \mathbb{R}$	Position dependent friction due to the input shaft
$\tau_{\mathrm{r}}(\theta) \in \mathbb{R}$	Position dependent friction due to the output shaft

gear alone and $\alpha_{gear} \in \mathbb{R}$ is the gear ratio of the harmonic drive from input to output velocity. Practically, the total inertia only depends on the input shaft inertia since the gear ratio is 1/100. In the absence of external forces, the equation of dynamics is

$$B\ddot{\theta} = \tau_{friction}(\theta, \dot{\theta}) + \tau_m, \tag{3.2}$$

where $\theta \in \mathbb{R}$ is the rotor position with respect to the stator. $\tau_m \in \mathbb{R}$ is the electromagnetic torque. The frictional torque $\tau_{friction}(\theta, \dot{\theta}) \in \mathbb{R}$ can be separated into the motor shaft and output shaft term as well as the velocity or position dependent terms leading to

$$\tau_{friction}(\theta, \dot{\theta}) = \tau_v(\dot{\theta}_{input}) + \tau_{r,input}(\theta_{input}) + \tau_v(\dot{\theta}) + \tau_r(\theta) \tag{3.3}$$

where the terms are defined in Table 3.1.

The motor velocity and the output velocity are related by the fixed gear ratio $\dot{\theta} = \alpha_{\mathrm{gear}}\dot{\theta}_{\mathrm{input}}$. Hence, only one velocity dependent term is kept (that accounts for both). The total frictional effects are consequently written:

$$\tau_{\mathrm{friction}}(\theta, \dot{\theta}) = \tau_{\mathrm{r,input}}(\theta_{input}) + \tau_{\mathrm{v}}(\dot{\theta}) + \tau_{\mathrm{r}}(\theta). \tag{3.4}$$

Using the velocity relation between $\dot{\theta}$ and $\dot{\theta}_{\mathrm{input}}$, the motor dynamics are

$$B\ddot{\theta} = \tau_{\mathrm{v}}(\dot{\theta}) + \tau_{\mathrm{r,input}}(\alpha_{\mathrm{gear}}^{-1}\theta) + \tau_{\mathrm{r}}(\theta) + \tau_{\mathrm{m}} \tag{3.5}$$

Description	Unit	Symbol
Inertia	kilogram meter square	$[kgm^2]$
Motor constant	Newton meter per ampere	$[Nm/A]$
Static friction torque	Newton meter	$[Nm]$
Viscous friction torque	Newton meter per radian per second	$[Nm/(rad/s)]$

Table 3.2: Parameters to be identified

where $B \in \mathbb{R}$ is the total motor inertia, $\theta \in \mathbb{R}$ is the output shaft position w. r. t. some arbitrary origin. $\tau_{\mathrm{v}}(\dot{\theta}) \in \mathbb{R}$ is the velocity dependent friction torque due to input and output viscous effects. $\tau_{\mathrm{r}}(\theta) \in \mathbb{R}$ (resp. $\tau_{\mathrm{r,input}}(\alpha_{\mathrm{gear}}^{-1}\theta) \in \mathbb{R}$) is the friction torque depending on the output (resp. input) shaft position.

3.2 Parameter identification

The unknown parameters of equation (3.5) (listed in table 3.2) must be either identified or neglected. In case of large uncertainties it is better to neglect frictional terms rather than over compensating them. Indeed, the energy introduced to compensate the friction may lead to the loss of mechanical passivity [113].

To identify the motor parameters of Table 3.2, several experiments are conducted:

- constant velocity square waves (for velocity dependent friction)
- constant torque impulse (for inertia modeling)
- constant velocity with Coulomb and viscous friction compensation (for ripple identification)

Inertia and torque constant The inertia and the motor electromagnetic constant (current to torque relationship) are linearly dependent in the dynamic equations. Therefore, either the inertia or the torque constant must be measured externally. The torque constant was determined by a direct torque measurement at the motor output shaft and is assumed to be constant among all the motors. The inertia was obtained from a current step response experiment, based on the model

$$B\ddot{\theta} = \tau_{\mathrm{m}}, \tag{3.6}$$

where $B \in \mathbb{R}$ is the inertia along the rotation axis, $\theta \in \mathbb{R}$ is the position of the motor shaft w. r. t. some arbitrary origin and $\tau_{\mathrm{m}} \in \mathbb{R}$ is the electromagnetic torque. This identification neglects the viscous friction and the stick-slip friction. The inertia value obtained by this method is comparable to the value obtained from the CAD data.

Table 3.3: Parameters of the friction model

Parameter	Unit	Value
γ_1	$[rad/s]^{-1}$	10
γ_2	$[Nm]$	0.5586
γ_3	$[Nm][rad/s]^{-1}$	0.0356

Friction At constant velocity, one can write (under the assumption that the friction is uniquely velocity dependent):

$$0 = \tau_{\mathrm{v}}(\dot{\theta}) + \tau_{\mathrm{r,input}}(\alpha_{\mathrm{gear}}^{-1}\theta) + \tau_{\mathrm{r}}(\theta) + \boldsymbol{\tau}_{\mathrm{m}} \tag{3.7}$$

where $\theta \in \mathbb{R}$ is the position of the motor shaft w. r. t. some arbitrary origin. $\tau_{\mathrm{v}}(\dot{\theta}) \in \mathbb{R}$ is the velocity dependent friction torque due to input and output viscous effects. $\tau_{\mathrm{r}}(\theta) \in \mathbb{R}$ (resp. $\tau_{\mathrm{r,input}}(\alpha_{\mathrm{gear}}^{-1}\theta) \in \mathbb{R}$) is the friction torque depending on the output (resp. input) shaft position and $\tau_{\mathrm{m}} \in \mathbb{R}$ is the electromagnetic torque.

Therefore, the friction parameters can be estimated for a given velocity $\dot{\theta}$ by driving at different constant speeds (as depicted in Fig. 3.3a). The steady-state motor torque for each velocity is obtained by an average filter applied to a few motor periods (the position dependent input and output torques $\tau_{\mathrm{r,input}}, \tau_{\mathrm{r}}$ are periodic) and repeating the measurements with different speeds leads to the Figure 3.3b.

To maintain the central symmetry and provide smoothness, the friction model is selected as

$$\hat{\tau}_{friction}(\dot{\theta}) = atan(\gamma_1\dot{\theta})\gamma_2 + \gamma_3\dot{\theta}, \tag{3.8}$$

where $\hat{\tau}_{\mathrm{friction}}(\dot{\theta}) \in \mathbb{R}$ is the estimated friction torque at a given velocity $\dot{\theta}$. The position dependent terms are neglected. The parameters γ_1, γ_2 and γ_3 for one specific motor are reported in Table 3.3.

Ripple The motor ripple (periodic disturbances) is generated by a magnetic or a mechanical effect and therefore is mainly position dependent. A compensation for the magnetic ripple is proposed and implemented in [114]. Bearing friction models and compensation schemes are discussed in [57] and harmonic drive specific friction is treated in [115]. Because two bearings are used (the motor shaft bearings and the output shaft bearing), two periodic disturbances appear on the motor torque. It is possible to cancel or at least to reduce the disturbances by applying a correct feedforward signal. In Figure 3.4a and 3.4b, 10 measurements with the same desired velocity are depicted and confirm the repeatability of the disturbances. In each of them the measurement was triggered on the same motor position. The measurements demonstrate that the position dependent friction effects are strongly repeatable.

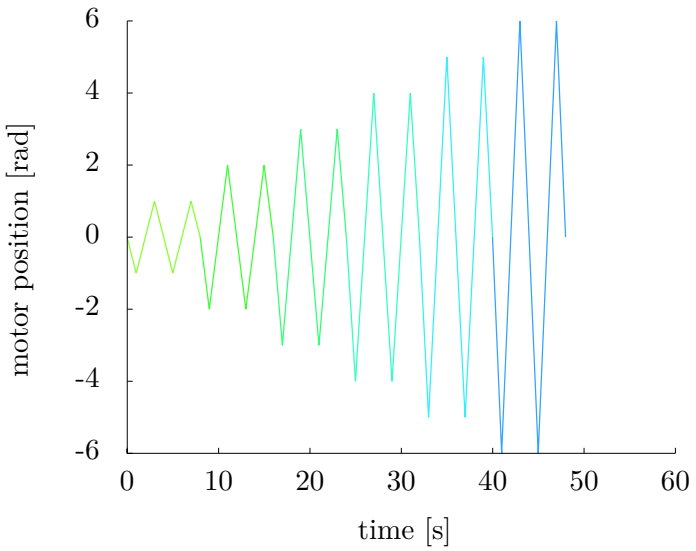

(a) Position profiles used to estimate the friction parameter (Piecewize constant velocity).

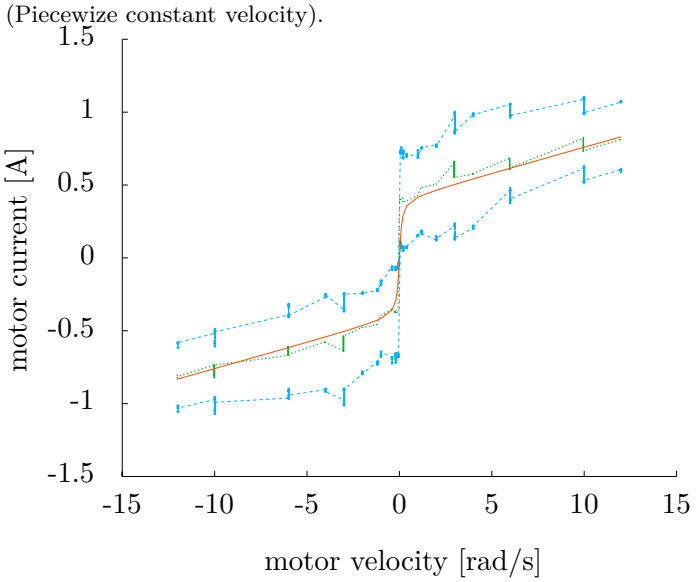

(b) Friction curve. The green (dotted center) is the average, the light blue lines are minimum and maximum (dashed top/bottom) and the red curve is the curve of the selected friction model (solid)

Figure 3.3: Experiment and results for the motor friction estimation

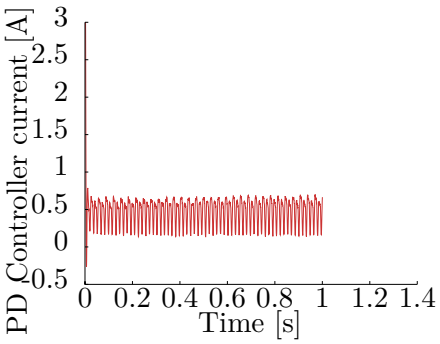

(a) Measured motor torque at a fixed velocity (using a simple PD controller)

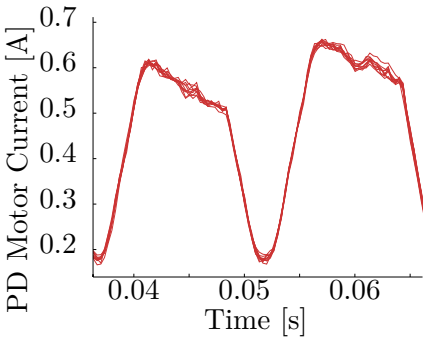

(b) Close view on 10 measures of the motor torque at a fixed velocity (using a simple PD controller)

Figure 3.4: Experiment: commanded torque for constant velocity motions

In Figure 3.5a, two measurements with the different desired velocities $\dot{\theta} = 1$ rad/s and $\dot{\theta} = 0.5$ rad/s are depicted and confirm that the disturbance is position dependent.

In order to assess the performance of the compensation is it necessary to quantify the disturbance. Due to its periodicity, a frequency analysis seems appropriate to analyze the motor recordings. Figure 3.5b shows the initial frequency distribution of the perturbation for the two desired velocities $\dot{\theta} = 1$[rad/s] and $\dot{\theta} = 0.5$[rad/s]. As expected the main frequency of the perturbation is equal to the motor rotation frequency, and the frequencies are clearly identifiable.

From those experiments, it can be concluded that the repeatability of the disturbance is excellent and its phase only depends on the motor position. Moreover, the reduction of the amplitude of the disturbance at the motor rotation frequency is selected to quantify the results (first harmonic removal/attenuation).

To compensate for disturbances, a feedforward term can be added to the controller action. The frequency and phase are directly given by the motor velocity but the amplitude is not known. As mentioned previously, the amplitude estimation must be conservative to avoid introducing potentially destabilizing energy.

3.3 Conclusion

Fig. 3.6b and Fig. 3.6a show the reduction of the torque disturbance amplitude in the frequency and in the time domains. Although hard to perceive in time domain, the attenuation is clearly visible in the frequency domain (as well as simply hearing the motor noise).

The small size of the motor and gear boxes inevitably introduce large

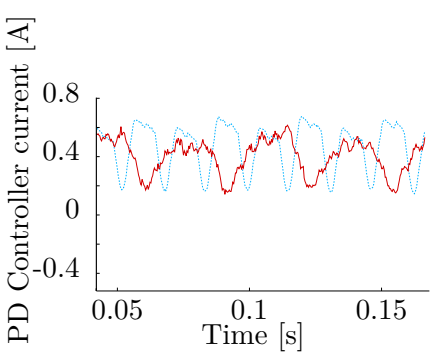

(a) Motor torque measured at two different constant speeds. The light blue dashed curved is obtained with a higher velocity as the red solid curve.

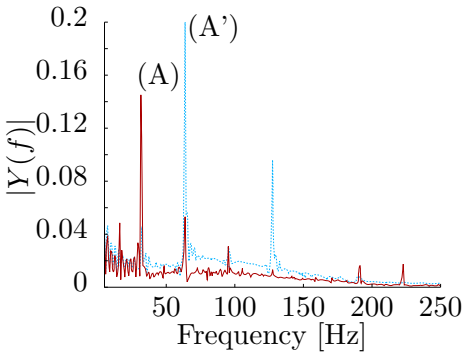

(b) Frequency decomposition at two different constant speeds. The light blue dashed curved is obtained with a higher velocity as the red solid curve. The main disturbance peak (A) is clearly shifted to the right (A').

Figure 3.5: Experiment: commanded torque for a constant velocity motion (time and frequency domains)

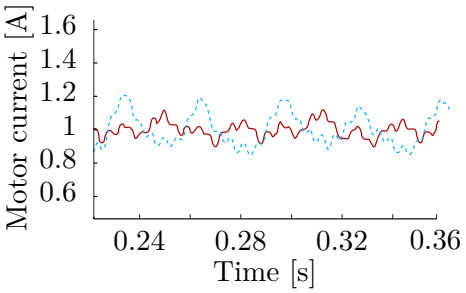

(a) PD controller desired torque (before compensator) without (light blue dashed) and with (red solid) the friction compensator

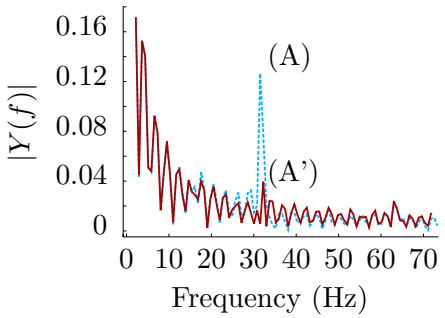

(b) Frequency decomposition without (light blue, dashed, above) and with (red, solid, below) the friction compensator

Figure 3.6: Experiment: resulting controller torque command in time and frequency domains after compensation

friction effects w. r. t. to their output torques (compared to a kW sized motor). However, different compensation mechanisms can benefit from the repeatability of the disturbances. A simple feedforward term can suppress, if not attenuate, most of the disturbances. Based on a rich literature of industrial applications, a compensation mechanism has been successfully designed and applied to the motors. Several experiments and analyses confirmed the benefit of the approach.

Despite the success of the method, some limitations must be stated; thanks to the high control frequency of 3kHz as well as the high quality of the motors and sensors, very high position controller gains can be used thus the benefit of the compensation is limited when the motor is used in position mode. Moreover, it must be noted that the compensation might lead to some noise or instability if the compensation is excessive (and consequently injecting more energy than the mechanism and the controller can dissipate). Nonetheless, the gain is appreciable when the motor is used as a torque source since the produced torque is closer to the desired one (reduced dead zone). It allows to reduce the controller effort (in tendon force control mode) since the forward model is more accurate and thus, indirectly, increases the system accuracy.

4 Tendon model

Several adjustable stiffness mechanisms are reported in [116]. In the hand of the Hand Arm System, tendons are used to carry the motor torque to the joint torque. But, because tendons can only pull and never push, they are used in an antagonistic configuration as depicted in Figure 4.1.

Besides the benefit of looking strongly anthropomorphic, the antagonistic tendon actuation allows to circumvent the issues of tendon slackening, change of tendon path length and routing complexity. Moreover, the use of nonlinear spring mechanism offers the possibility to adjust the joint stiffness (cf. Fig. 4.2). Although several methods can be used to control the system, they all require position or force control of the tendons (at least indirectly, e. g. to limit the tendon forces).

The beginning of this section describes the variable stiffness mechanisms, derives a mathematical model and verifies the model with a calibration experiment. Once the variable mechanism is modeled, the tendon is mounted in conditions similar to the final assembly (i. e. same number of pulleys) to estimate the quality of control that could be achieved. The experiment allows to measure the friction of the guidings and latter estimate the joint friction. The friction behavior with different mounting conditions is studied because a proper tendon force control is paramount to the successful operation of most of the controllers.

4.1 Mechanical design

This section is based on the sensor design by Werner Friedl that has been presented in [3]. The selection process of a tendon material is explained, followed by the geometrical description of the adjustable stiffness mechanism.

Tendon material selection The choice of the tendon material is critical for the design, since it imposes pulley geometries and radii, as well as the type of sliding surfaces that can be used. In the case of the Hand Arm System, a polymer fiber known commercially as Dyneema®[1] is selected over steel or vectran[2]. The main reason is its durability even for small pulley radii(cf. Fig. 4.3). Moreover it offers a termination technique called splicing (cf. Fig. 4.4) allowing to perform on site terminations. Although apparently accessory, this is extremely relevant when considering the time needed to assemble, maintain, and repair the system.

[1] Dyneema®is the commercial name of a strand of Ultra-high-molecular-weight polyethylene fibers.

[2] Vectran is a manufactured fiber of aromatic polyester.

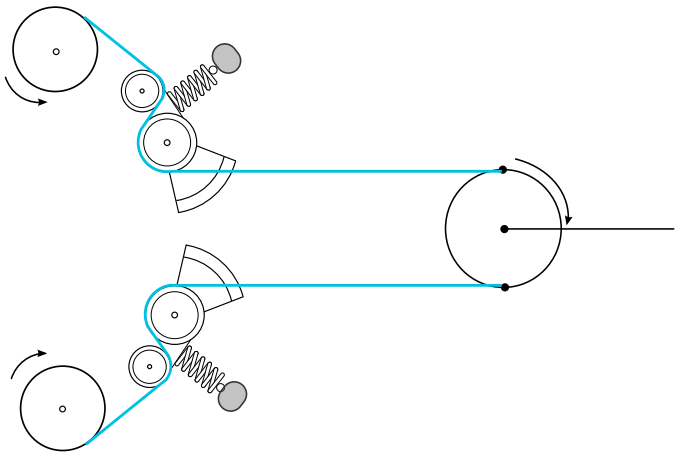

Figure 4.1: Antagonistic arrangement of the tendons allowing to move the joint and adjust its stiffness

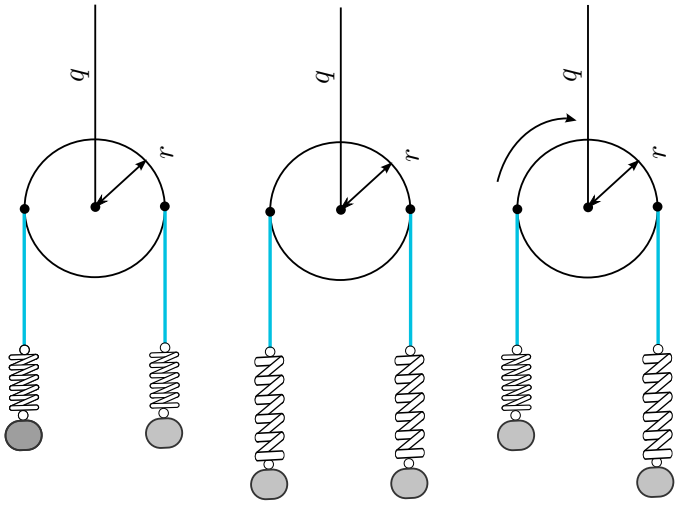

(a) (b) (c)

Figure 4.2: (a) A balanced set of forces is creating no joint torque. (b) Increasing the co-contraction of the tendons increases the link joint stiffness. (c) An unbalanced set of forces creates a torque

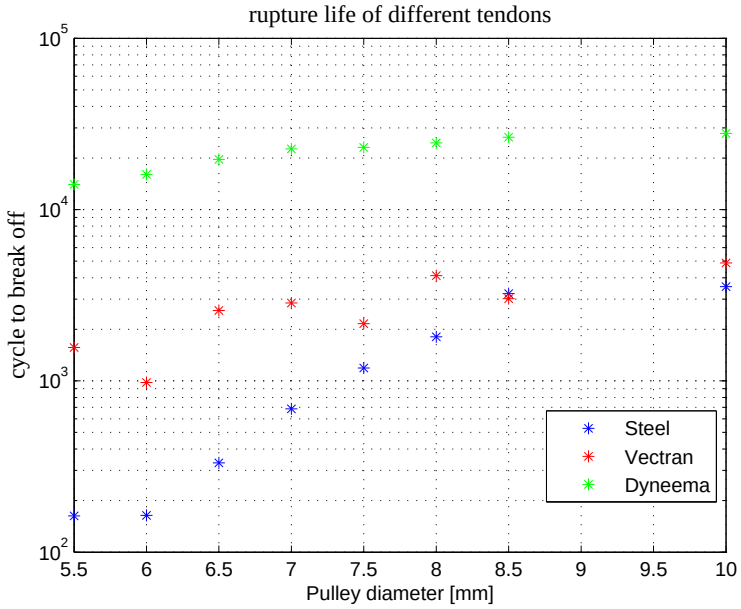

Figure 4.3: Durability test of different tendon material depending on the pulley radius

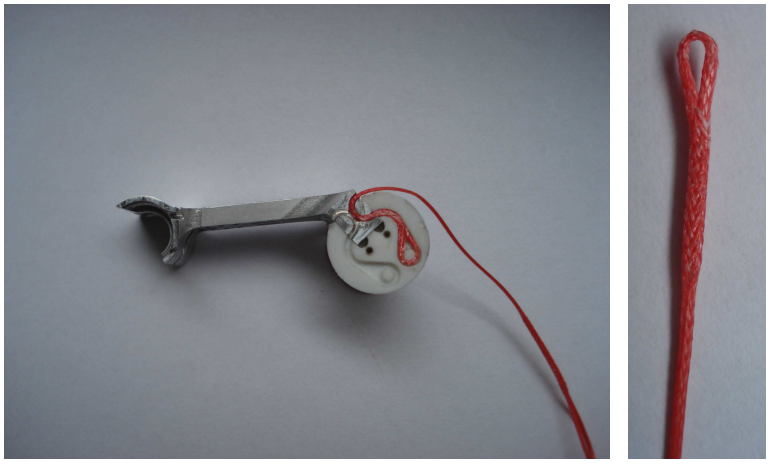

(a) Mounting of a tendon

(b) Splice of a tendon)

Figure 4.4: Splicing technique used to terminate the tendons

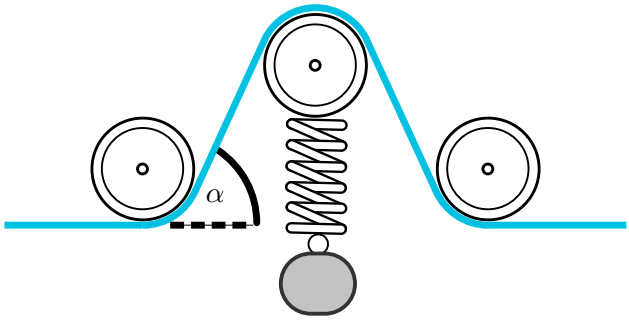

Figure 4.5: Original concept: tangent α mechanism

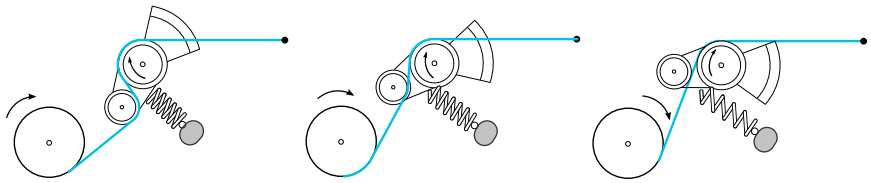

Figure 4.6: Geometry of the tendon force sensor: the stiffness is increasing from left to right

Geometrical Design The variable stiffness spring mechanism is based on the *tangent* α mechanism (cf. Fig. 4.5). The genuine design has been modified to minimize the number of pulleys and to replace the linear guiding by a rotational guiding. The resulting design is depicted in Fig. 4.6. The variables used through the modeling are reported in Table 4.1.

The length of the tendon in the mechanism (referred to as dL) is given with respect to the lever angle (referred to as θ_{lever}). The force characteristic and the tendon stiffness of one tendon are reported in Figure 4.7 (other tendons have different curves but the shape is imposed by the mechanism geometry).

Sensor Design To obtain a compact design a commercial Hall effect sensor is used off-axis (see Fig. 4.8a). The magnet attached to the lever sweeps over the hall effect sensor [117] and creates a magnetic field variation that is the measured quantity. The sensor provides a resolution of 12 bits at a frequency of 3 kHz. The sensor has a filter algorithm included which can be adjusted to reduce the noise level (at the cost of an increased hysteresis).

Calibration The tendon mechanisms must be calibrated because of the mounting variability, the variations in the sensor's sensitivity and the tolerances of the spring constant. The setup depicted in Fig. 4.8a is used to calibrate the sensors in place, therefore including the stiffness of the tendon material in the measurement.

Description	Symbol
θ_{lever}	Angle of the lever
$dL(\theta_{lever})$	Length of tendon from the motor pulley to the fixed pulley
$[x_{motor}, y_{motor}]$	Coordinates of the motor pulley center
$[x_{fixed,pulley}, y_{fixed,pulley}]$	Coordinates of the fixed pulley center
$[x_{lever}, y_{lever}]$	Coordinates of the lever pulley center
$[x_{spring}, y_{spring}]$	Coordinates of the spring fixed
K	Spring constant
R_{motor}	Radius of the motor pulley
R_{lever}	Radius of the lever pulley
$R_{fixed,pulley}$	Radius of the fixed pulley
K	Spring constant

Table 4.1: Parametrization of the spring mechanism

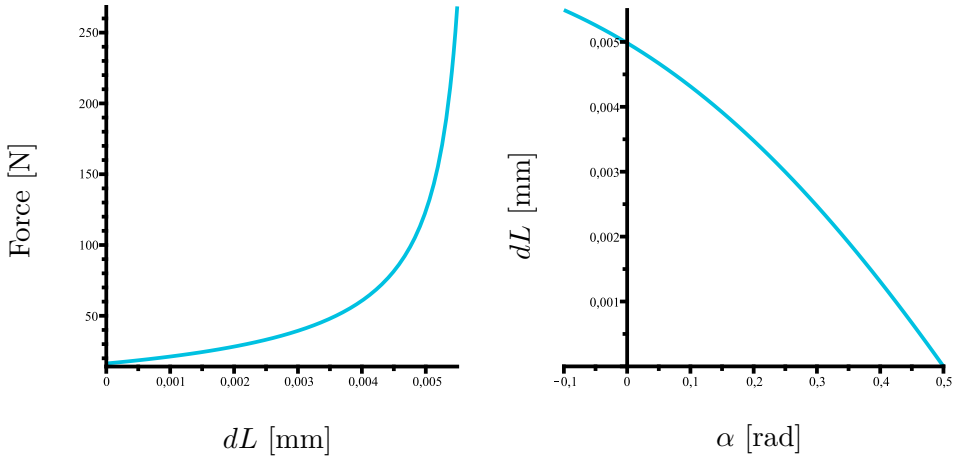

Figure 4.7: Model based mechanism characteristics

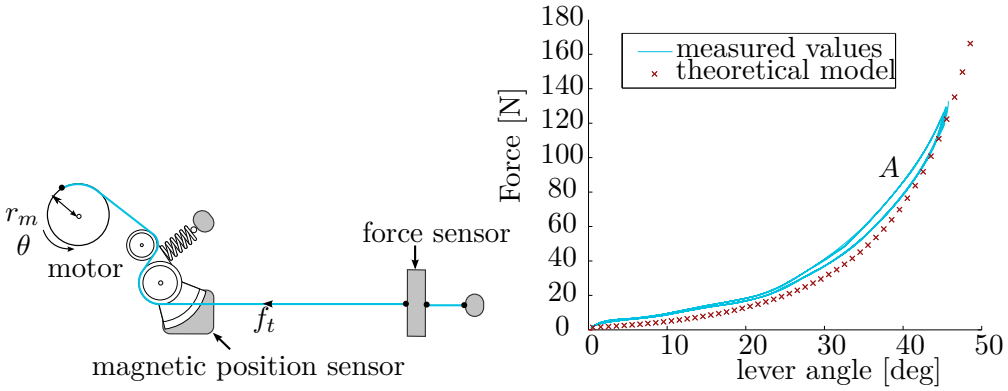

(a) Setup used for the tendon calibration

(b) Measured and model characteristic (position/force) of a tendon. (A) denotes a point where the hysteresis is about 10 N

Figure 4.8: Tendon force/stiffness calibration

The raw measurement of Figure 4.8b exhibits a good similarity with the model. The offset between the model and the measurement can be attributed to the spring constant mismatch and the friction in the lever mechanism. A more accurate fit can be obtained by adjusting the uncertain parameters (e. g. spring constant). Each individual sensor is calibrated after mounting to verify the magnetic sensor and the tendon mounting. Adjusted models are then approximated by polynomials that are used to transform the magnetic sensor output (increments) to the tendon force f_t[N], the tendon stiffness k_t[N/m] and the tendon length in the mechanism dL[m]. The polynomials are required to minimize the computation costs for the real-time implementation. One important element to note is the hysteresis cycle that reaches $10N - 20N$ at a force of about 70N (cf. Fig. 4.8b point (A)).

4.2 Guiding friction estimation

Through the measurement campaign, it appeared that the pulley guidings in the wrist and the palm are introducing a large static friction when used with the Dyneema®tendons. In order to qualify, quantify, and propose a model, a new set of experiments (depicted in Fig. 4.9) was conducted with different pulley radii and tendon diameters and materials. Figure 4.10 show that bending the dyneema fibers around the pulley requires a larger force than for the steel cables. Moreover, the friction is increasing when the bending diameters are diminishing. The friction behavior shows an independence with respect to the tendon speed (in the range of the expected tendon velocities).

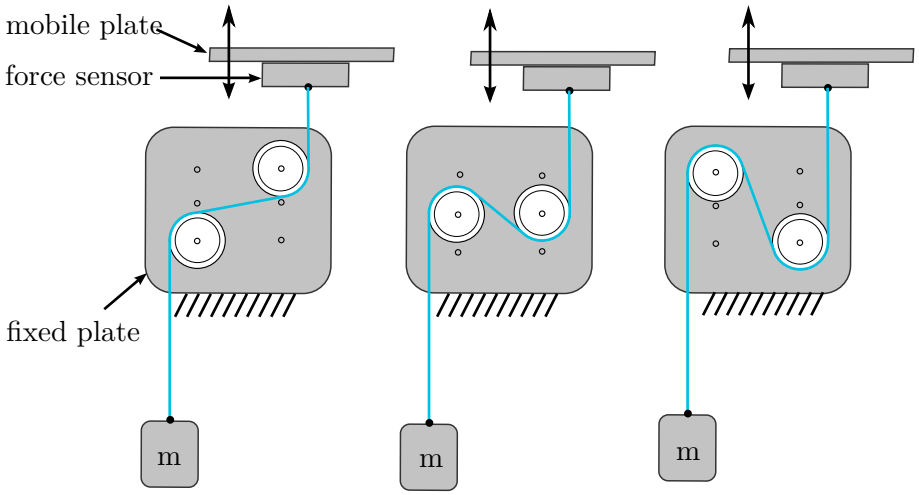

Figure 4.9: Experiment for guiding friction estimation

It appears that the tendon friction force $F_{friction} \in \mathbb{R}^+$ can be approximated by equation,

$$F_{friction} = C_0(1 - e^{-C_1\alpha}), \tag{4.1}$$

where $\alpha \in \mathbb{R}^+$ is the total bending angle and $(C_0, C_1) \in \mathbb{R}^2$ are calibration constants.

The measurements have been performed with a special tendon pulling machine [118] that offers controlled displacements and accurate force measurements. In all tests the friction force is estimated to be the steady-state pulling force during a saw shaped motion. Other experiments have been performed to compare the sliding friction to the pulley friction so as to give all needed information to the mechanical designers. The tables are available to the mechanical teams in order to decide when to use pulleys (that requires space) or sliding surfaces (more compact but limited to small bending angles). Figure 4.10 and 4.11 are the graphs of such tables.

4.3 Conclusion

This section has presented the tendon stiffness mechanism used for each of the 38 tendons of the forearm. The mechanical construction is an improvement over the original tangent α mechanism in terms of size and complexity. The tendon material has been selected to provide a long lifetime as well as to cope with the small bending radii. It has been experimentally verified that the model based stiffness curve of the mechanism exhibits a good match with the measures. The discrepancies between the theoretical model and the measure are related to the imprecision of the spring constant (given by the manufacturer). The stiffness of the tendon material contributes to the over-

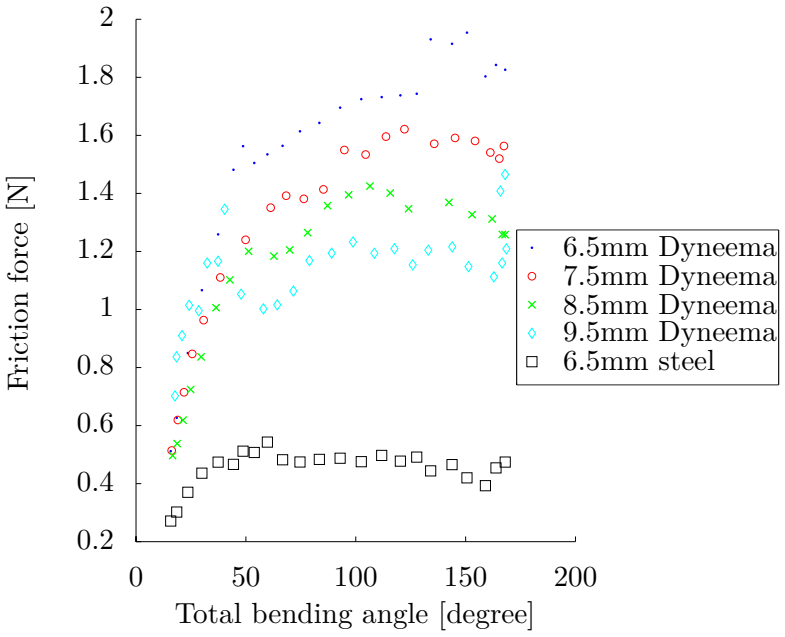

Figure 4.10: Friction force for a single tendon depending on the total bending angle. Pulley diameters and several sliding materials are compared

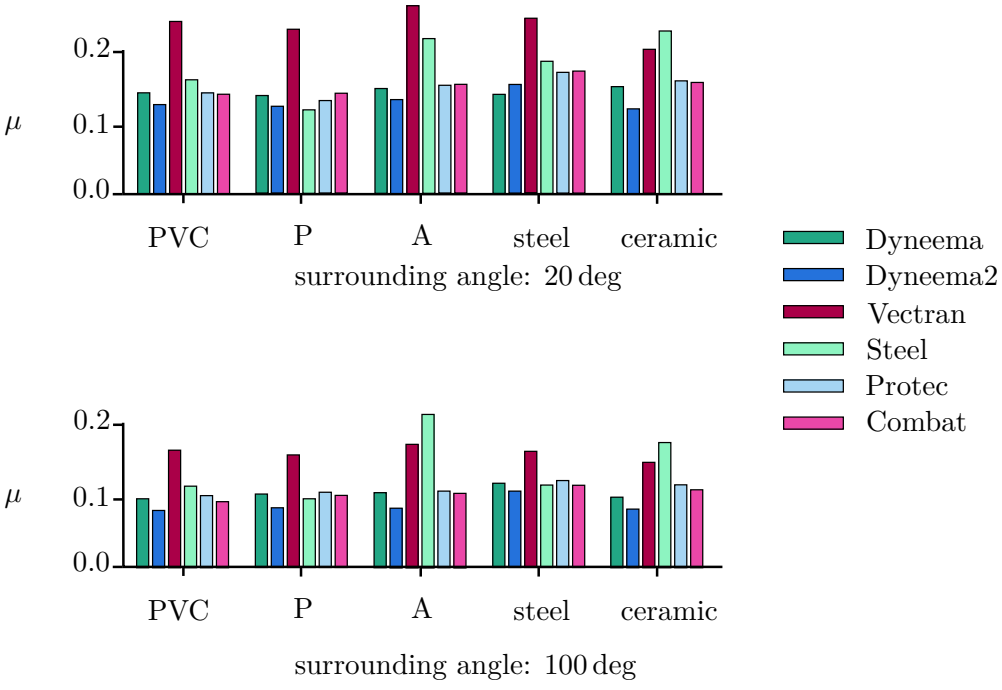

Figure 4.11: Friction coefficient in a sliding experiment for a single tendon depending on the material combinations. P (resp. A) stands for a low friction polymer similar to the one used for the joints (resp. an aluminium alloy).

all stiffness of the mechanism. Therefore, the calibration is performed on the mounted tendon. The real-time implementation uses calibration polynomials to improve the measurement accuracy. A set of characterization experiments has been conducted in order to provide a clear overview of the friction properties of the tendon and the experimental results have been used to establish a model of the tendon friction in the case of rolling and sliding. The model is available to the mechanical engineers. So they have the information needed to decide between the different guiding options.

5 Finger model

In this chapter the mechanical modeling of the fingers is described. First, the homogeneous transformation matrices are derived from the CAD (Computer Aided Design) data. The dynamic model is easily obtained from a symbolic calculation tool, either from the energy expression and the Lagrange method or from the Newton-Euler method. The tendon coupling is presented in detail and is one major novelty of the design. Each of the five fingers has a specific design, but their types can be grouped as follows (cf. Fig. 5.1):

- Base of the thumb (MC: Metacarpal joint, also called TMC: trapezoid metacarpal joint).
- Base of the index, middle, ring, and fifth fingers(MC: Metacarpal joint).
- Medial and distal joints of the thumb, index, middle fingers (PIP: proximal inter-phalangeal and DIP: distal inter-phalangeal joint).
- Medial and distal joints of the ring and fifth fingers (PIP: proximal inter-phalangeal and DIP: distal inter-phalangeal joint).
- Hematometacarpal joint of the fifth finger (HMC: hematometacarpal joint).

Several joint types are used for the fingers. The base joint is a hyperboloid joint (cf. Fig. 5.2) and the PIP and DIP joints are hinges joints (cf. Fig. 5.3).

Those mechanisms have been carefully designed to ensure a maximal robustness while satisfying the functional requirements [98]. The base of the thumb is special since it is using a tensegrity[1] structure to provide an increased torque. The Hematometacarpal joint (HMC) is also very particular since it is realized by a four bar linkage to emulate the anatomical motion. In order to reduce the number of actuators and fit in the forearm, the PIP and DIP joints of the ring and fifth fingers are coupled. Despite the tendon routing differences, the kinematic structures of each finger are identical. Only the bones are different in size and shape.

[1]Tensegrity, tensional integrity or floating compression, is a structural principle based on the use of isolated components in compression inside a net of continuous tension, in such a way that the compressed members (usually bars or struts) do not touch each other and the prestressed tensioned members (usually cables or tendons) delineate the system spatially.

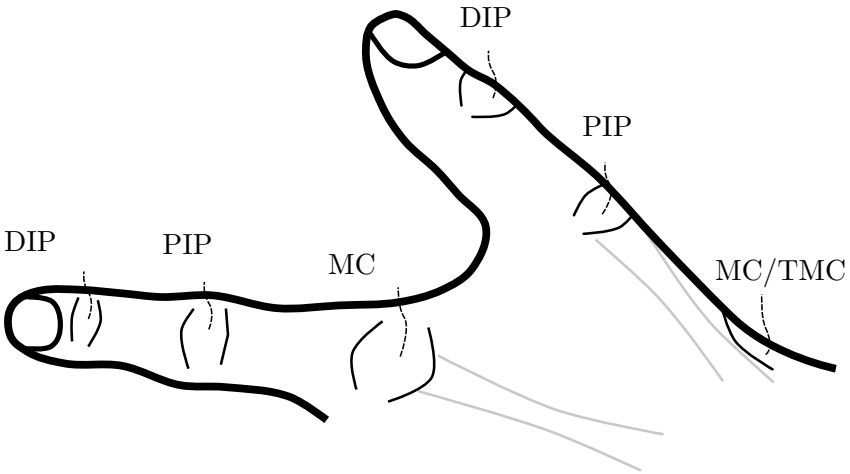

Figure 5.1: Joint names

Figure 5.2: Hyperboloid joint of the finger base

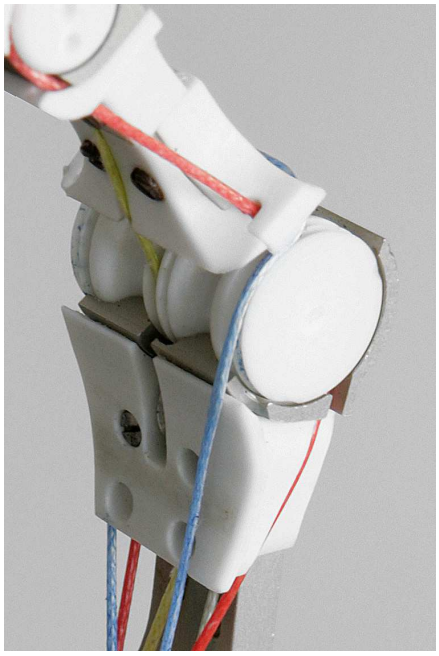

Figure 5.3: Dislocatable hinge joint for the PIP and DIP joints

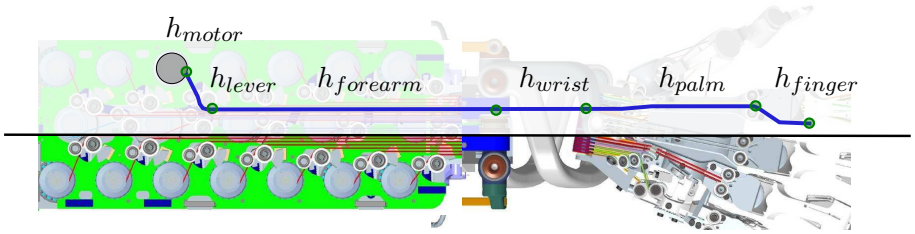

Figure 5.4: Tendon routing of the index finger through the complete forearm

5.1 Tendon routing

The fingers of the hand of the Hand Arm System are actuated by tendons. The tendons are pulled by electromotors that are placed in the forearm. Therefore, the tendons are running in the forearm, crossing the wrist, guided into the palm and finally routed in the finger. The tendons are transmitting the forces of the motors to the joints, thus being one of the most critical component. In order to control the joint torques the transmission chain must be analyzed and modeled. The tendon paths can be divided into six sections (cf. Fig. 5.4).

From figure 5.4 the length of tendon h^i ($i \in [1 \dots 38]$) is

$$h^i = h^i_{motor} + h^i_{lever} + h^i_{forearm} + h^i_{wrist} + h^i_{palm} + h^i_{finger}, \forall i \in [1 \dots 38] \quad (5.1)$$

where:

- h^i_{motor} represents the length of tendon i in the forearm (constant w. r. t. the robot configuration)(cf. Fig. 5.4).
- $h^i_{forearm}$ represents the length of tendon i in the forearm (constant w. r. t. the robot configuration)(cf. Fig. 5.4).
- h^i_{lever} represents the length of tendon h^i in the lever mechanism (depending on the tendon force of the finger)(cf. Fig. 5.4).
- h^i_{wrist} represents the length of tendon h^i in the wrist (depending on the joint angle of the wrist)(cf. Fig. 5.4).
- h^i_{palm} represents the length of tendon h^i in the palm (constant w. r. t. the robot configuration)(cf. Fig. 5.4).
- h^i_{finger} represents the length of tendon h^i in the finger (depending on the joint angle of the finger)(cf. Fig. 5.4, cf. Fig. 5.5).

The length of tendon in the forearm and the palm are independent of the robot configuration and will consequently be *neglected/hidden* in the rest of the thesis. It is interesting to note that, although those sections are of constant length, they depend on the tendon considered. The default length induces a serial stiffness that results in a softer tendon if it is longer. If $E_{dyneema}$[N/m] denotes the Young's modulus of the Dyneema®and $l^i_0, \forall i \in [1 \dots 38]$ is the default length of tendon, the tendon stiffness is given by $k^i_t = E_{dyneema} S / l^i_0, \forall i \in [1 \dots 38]$, where S is the cross-sectional area. It should be noted that the stiffness of the tendon is naturally included in the calibration process since it is performed once the tendon is mounted in the forearm.

5.2 Index, middle, and ring fingers

In this section the modeling of the index, middle, and ring fingers is presented. Due to their specificity, the modeling of the thumb and the fifth finger are deferred and are treated in separate sections.

5.2.1 Kinematic model

The index finger is modeled as a serial kinematic robot. The frames and the joint angle labels relevant for the model are depicted in Fig. 5.6. Table 5.1 reports the numerical values obtained from the CAD. $c_{xi} \in \mathbb{R}, i \in [0..3], x \in [1..5]$ (resp. $s_{xi} \in \mathbb{R}$) is the cosine (resp. the sine) of the joint angle i of finger x. Using some linear algebra, the partial and complete homogeneous transformations are obtained as:

$$ {}^j_i\boldsymbol{T}_x = \prod_{k=i}^{k=j-1} ({}^{k+1}_{k}\boldsymbol{M}_x), \forall (i,j) \in \mathbb{N}^2, \tag{5.2} $$

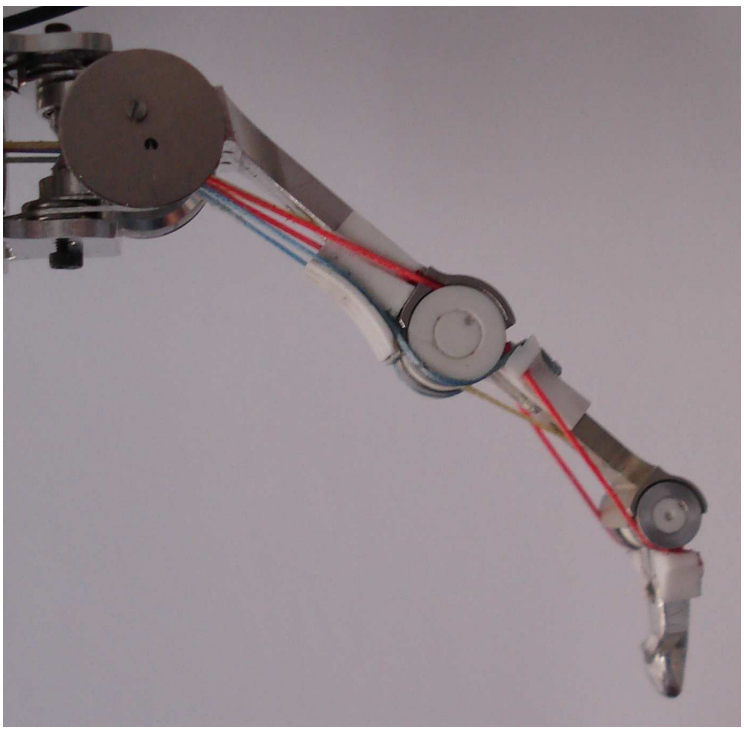

Figure 5.5: Index finger of the Hand Arm System

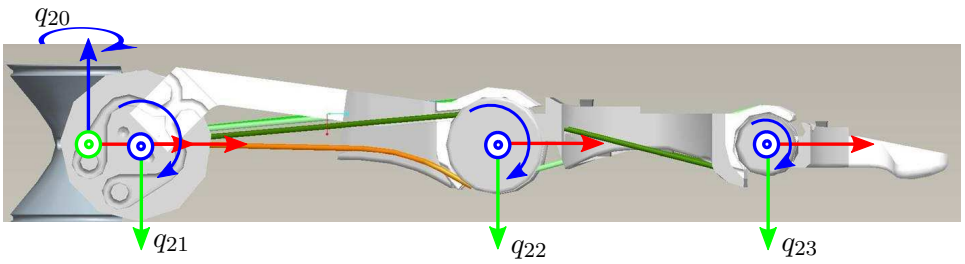

Figure 5.6: Frame definition of the index finger of the Hand Arm System (side view)

$$
{}^{1}_{0}\boldsymbol{M}_{index} = \begin{bmatrix} c20 & -s20 & 0 & 0 \\ s20 & c20 & 0 & 0 \\ 0 & 0 & 1 & 0 \\ 0 & 0 & 0 & 1 \end{bmatrix}
{}^{2}_{1}\boldsymbol{M}_{index} = \begin{bmatrix} 1 & 0 & 0 & 0 \\ 0 & 0 & -1 & 0 \\ 0 & 1 & 0 & 0 \\ 0 & 0 & 0 & 1 \end{bmatrix}
{}^{3}_{2}\boldsymbol{M}_{index} = \begin{bmatrix} 1 & 0 & 0 & 0.006 \\ 0 & 1 & 0 & 0 \\ 0 & 0 & 1 & 0 \\ 0 & 0 & 0 & 0 \end{bmatrix}
$$

$$
{}^{4}_{3}\boldsymbol{M}_{index} = \begin{bmatrix} c21 & -s21 & 0 & 0 \\ s21 & c21 & 0 & 0 \\ 0 & 0 & 1 & 0 \\ 0 & 0 & 0 & 1 \end{bmatrix}
{}^{5}_{4}\boldsymbol{M}_{index} = \begin{bmatrix} 1 & 0 & 0 & 0.04038 \\ 0 & 1 & 0 & 0 \\ 0 & 0 & 1 & 0 \\ 0 & 0 & 0 & 1 \end{bmatrix}
$$

$$
{}^{6}_{5}\boldsymbol{M}_{index} = \begin{bmatrix} c22 & -s22 & 0 & 0 \\ s22 & c22 & 0 & 0 \\ 0 & 0 & 1 & 0 \\ 0 & 0 & 0 & 1 \end{bmatrix}
{}^{7}_{6}\boldsymbol{M}_{index} = \begin{bmatrix} 1 & 0 & 0 & 0.0298 \\ 0 & 1 & 0 & 0 \\ 0 & 0 & 1 & -0.005 \\ 0 & 0 & 0 & 1 \end{bmatrix}
$$

$$
{}^{8}_{7}\boldsymbol{M}_{index} = \begin{bmatrix} c23 & -s23 & 0 & 0 \\ s23 & c23 & 0 & 0 \\ 0 & 0 & 1 & 0 \\ 0 & 0 & 0 & 1 \end{bmatrix}
{}^{9}_{8}\boldsymbol{M}_{index} = \begin{bmatrix} 1 & 0 & 0 & 0.00201 \\ 0 & 1 & 0 & 0 \\ 0 & 0 & 1 & -0.0007 \\ 0 & 0 & 0 & 1 \end{bmatrix}
$$

Table 5.1: Transformations from index base to index fingertip

where i, j are the indices of the frames between which the transformation is calculated. ${}^{j}_{i}\boldsymbol{T}_{x} \in \mathbb{R}^{4\times4}$ is the homogeneous transformation between the frames of index $i \in \mathbb{N}$ and $j \in \mathbb{N}$ of finger x. The matrices ${}^{k+1}_{k}\boldsymbol{M}_{x} \in \mathbb{R}^{4\times4}$ are the partial transformations of the bones or of the joints (in homogeneous coordinates) of the finger x at index k. For example, the transformation from the index base ($x =$ index and $i = 1$) to the index tip ($x =$ index and $j = 9$) is obtained as:

$$
{}^{9}_{0}\boldsymbol{T}_{index} = \prod_{k=0}^{8} ({}^{k+1}_{k}\boldsymbol{M}_{index}) \tag{5.3}
$$

5.2.2 Dynamic model

The Lagrangian L is obtained as $\mathcal{L} = \mathcal{T} - \mathcal{V}$, where $\mathcal{T}$ is the kinetic energy and $\mathcal{V}$ the potential energy due to the gravity. Considering that the forearm is fixed in space, the energy of the motor is reduced to the kinetic energy due to the rotor inertia. The Lagrangian is

$$\mathcal{T} = \frac{1}{2}\sum_{i=1}^{n} M_i v_i(q)^2 + \frac{1}{2}\sum_{i=1}^{n} B_i \dot{\theta}_i^2 + \mathcal{T}_g + \mathcal{T}_e, \tag{5.4}$$

where $n \in \mathbb{N}$ is the number of links, $M_i \in \mathbb{R}$ (resp. $B_i \in \mathbb{R}$) is the mass of the link $i \in \mathbb{N}$ (resp. the inertia of link $i \in \mathbb{N}$ expressed at the center of mass of the link). $v_i \in \mathbb{R}$ (resp. $\dot{\theta}_i \in \mathbb{R}$) is the velocity of the center of mass of link $i \in \mathbb{N}$ expressed in the world coordinates (resp. the rotational velocity of the link $i \in \mathbb{N}$ expressed in the world coordinates). $\mathcal{T}_g$ and $\mathcal{T}_e$ are the potential energy due to gravity and the potential energy due to the elastic storage. The elastic potential has the form $\mathcal{T}_e(\theta, q) = \frac{1}{2}\int k_t(h)h dh$, where $k_t(h)$ is the stiffness of the tendon and $h(\theta, q)$ is the elongation of the tendon.

The Coriolis and centrifugal terms are commonly neglected in hand modeling. This is mostly justified by the short length of the fingers and their small mass. However, in order to verify the assumption, several trajectories with or without the Coriolis and centrifugal terms have been simulated. The motor positions are fixed and the finger is initially deflected 0.1 rad in the second joint (flexion) and it is released at time t=0 s. As expected the finger oscillates and the inertial couplings are generating a motion of the distal links. The first joint is not influenced by the motion and therefore, is remaining at position $q_0 = 0$ rad. A damping of 0.1% was included in the joints. The curves reported in Fig. 5.7 are representing the differences of position in radians for each joint with and without accounting for the Coriolis and centrifugal terms. It can be seen that the simulation error is small compared to the accuracy of the sensors. Therefore, in this thesis, the Coriolis and centrifugal torque covectors are neglected. Similarily, the influence of gravity can be neglected w. r. t. the torques created by the tendons. Indeed, the complete finger mass is about 0.02 kg, with a center at about 0.01 m, which gives a torque of approximatively τ_q =0.02 kg×9.81 N×0.01 m = 0.002 Nm. It represents only 0.3 N to be shared on the base tendon forces.

5.2.3 Tendon coupling

Coupling matrices

The joints are driven by an antagonistic arrangment of tendons (cf. Fig. 5.9). Therefore, in absence of joint friction, the joint can be moved by placing the motors at the proper position (within the joint limits). However,

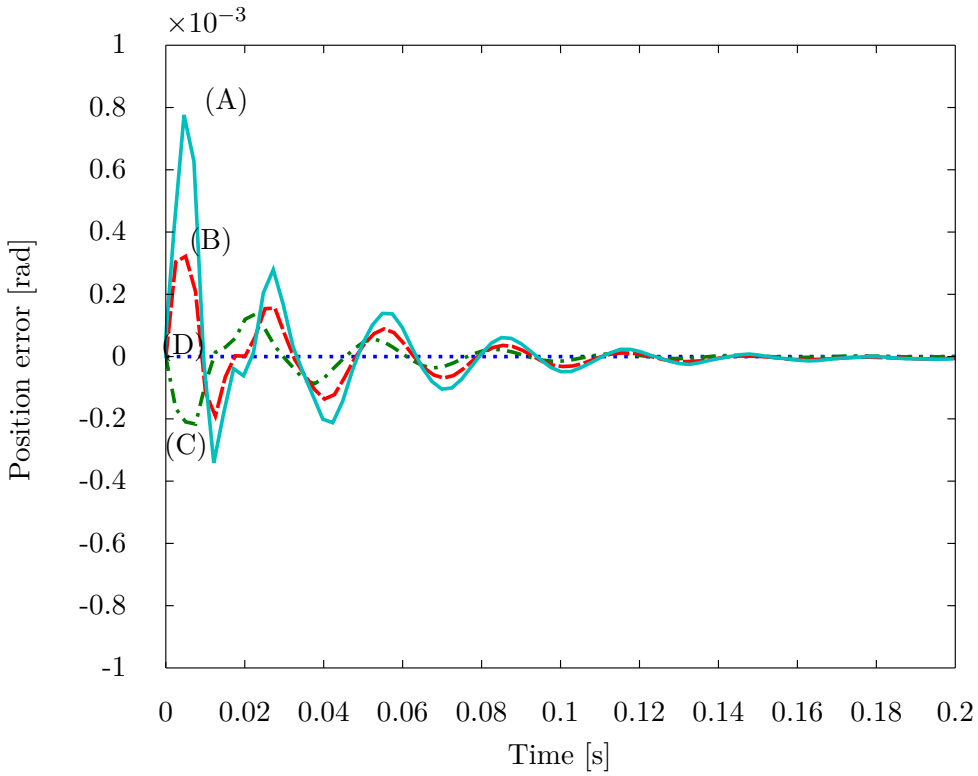

Figure 5.7: Simulation: influence of the Coriolis and centrifugal terms on the link trajectory. The curves illustrate the error between the full model and the simplified model. The base flexion (resp. PIP flexion, DIP flexion and base abduction/adduction) is the light light blue (A) curve (resp. red (B), green (C) and blue (D))

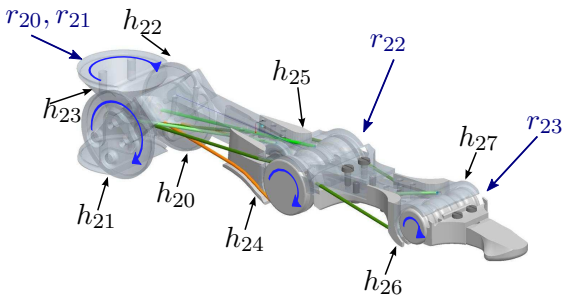

Figure 5.8: Names of the tendons and radii of the pullies of the index finger used to establish eq. (5.22).

without control, a motion of the PIP joint creates a motion of the DIP joint because the DIP tendons are rolling around the PIP joint (cf. Fig. 5.10). The tendon lengths in the finger h_{finger} are obtained from the joint pulley radii:

$$\begin{aligned}
h_{index,1}(\boldsymbol{q}) &= h_{0,index,0} + r_{20}q_{20} + r_{21}q_{21} \\
h_{index,2}(\boldsymbol{q}) &= h_{0,index,1} + r_{20}q_{20} - r_{21}q_{21} \\
h_{index,3}(\boldsymbol{q}) &= h_{0,index,2} - r_{20}q_{20} + r_{21}q_{21} \\
h_{index,4}(\boldsymbol{q}) &= h_{0,index,3} - r_{20}q_{20} - r_{21}q_{21} \\
h_{index,5}(\boldsymbol{q}) &= h_{0,index,4} + r_{22}q_{22} \\
h_{index,6}(\boldsymbol{q}) &= h_{0,index,5} - r_{22}q_{22} \\
h_{index,7}(\boldsymbol{q}) &= h_{0,index,6} + r_{22}q_{22} - r_{23}q_{23} \\
h_{index,8}(\boldsymbol{q}) &= h_{0,index,7} - r_{22}q_{22} + r_{23}q_{23}
\end{aligned} \tag{5.5}$$

where $h_{0,x,i}$, with $i \in [1 \dots 8]$ denotes the initial (arbitrary reference) tendon length in the finger x. $q_i \in \mathbb{R}, i \in [0 \dots 3]$ are the joint angles. $r_{ij} \in \mathbb{R}, (i,j) \in ([1 \dots 5] \times [0 \dots 3])$ are the pulley radii of finger i at joint j (cf. Fig. 5.8).

From the expression of the tendon lengths given in Eq. (5.22), the coupling matrix $\boldsymbol{P}(\boldsymbol{q}) \in \mathbb{R}^{m \times n}$ (for a finger with $n \in \mathbb{N}$ joints driven by $m \in \mathbb{N}$ tendons) is defined as

$$\boldsymbol{P}(\boldsymbol{q}) = \frac{\partial \boldsymbol{h}(\boldsymbol{q})}{\partial \boldsymbol{q}}. \tag{5.6}$$

Equation (5.6) also expresses the relationship between the tendons velocities and the joint velocities:

$$\dot{\boldsymbol{h}} = \boldsymbol{P}(\boldsymbol{q})\dot{\boldsymbol{q}} \tag{5.7}$$

The relation between the motor torques $\boldsymbol{\tau}_\theta \in \mathbb{R}^m$ and the joint torques $\boldsymbol{\tau}_q \in \mathbb{R}^n$ is simply obtained by expressing the work produced by the motors and the work produced by the joints and substituting eq. (5.7).

$$\boldsymbol{\tau}_q = \boldsymbol{P}(\boldsymbol{q})^T \boldsymbol{\tau}_\theta, \tag{5.8}$$

where $\boldsymbol{P}(\boldsymbol{q}) \in \mathbb{R}^{n \times m}$ is the coupling matrix, $\boldsymbol{q} \in \mathbb{R}^n$ is the joint position. $\boldsymbol{\tau}_q \in \mathbb{R}^n$ (resp. $\boldsymbol{\tau}_\theta \in \mathbb{R}^m$) is the joint torque covector (resp. the motor torque covector).

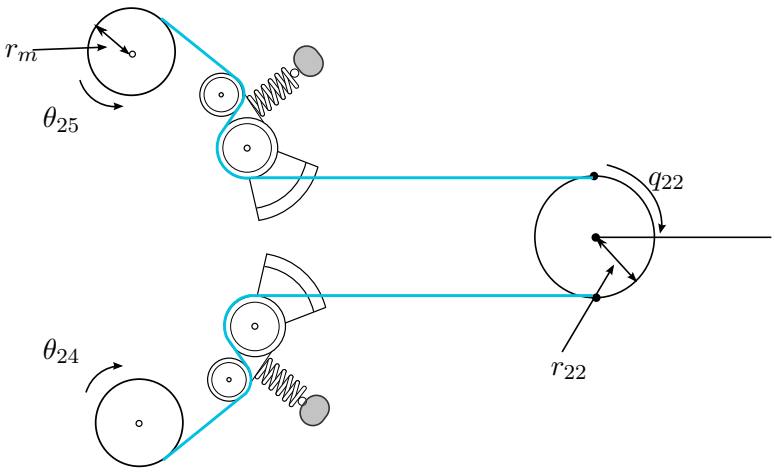

Figure 5.9: Antagonistic model of a joint. Two motors are pulling two tendons guided through the stiffness elements and drive the joint (courtesy of Jens Reinecke).

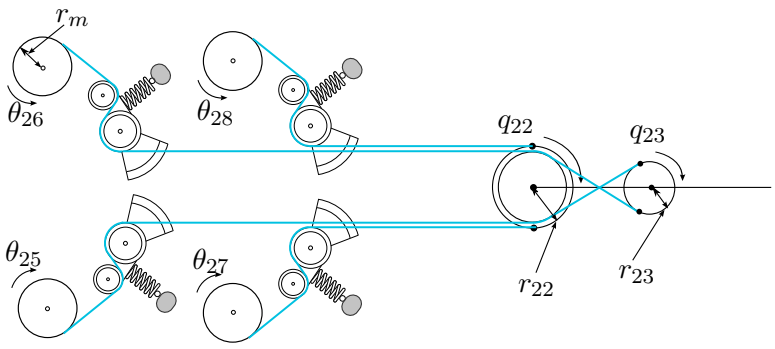

Figure 5.10: Example of the tendon guiding in the PIP and DIP. The total lengths of the tendons are simply obtained because the tendons are rolling on the pulleys.

Applied to the index finger, the coupling matrix is

$$\boldsymbol{P}_{index} = \begin{bmatrix} r_{20} & -r_{21} & 0 & 0 \\ -r_{20} & -r_{21} & 0 & 0 \\ r_{20} & r_{21} & 0 & 0 \\ -r_{20} & r_{21} & 0 & 0 \\ 0 & 0 & -r_{22} & 0 \\ 0 & 0 & r_{22} & 0 \\ 0 & 0 & r_{22} & -r_{23} \\ 0 & 0 & -r_{22} & r_{23} \end{bmatrix}, \tag{5.9}$$

where $(r_{20}, r_{21}, r_{22}, r_{23}) \in (\mathbb{R}^+)^4$ are the radii of the joint pulleys.

Stiffness transformation

The modification of the tendon stiffness modifies the joint stiffness. The joint stiffness matrix $\boldsymbol{K}_q(\boldsymbol{q}) \in \mathbb{R}^{n \times n}$ is by definition:

$$\boldsymbol{K}_q(\boldsymbol{q}) = \frac{\partial \boldsymbol{\tau}_q}{\partial \boldsymbol{q}}. \tag{5.10}$$

The joint torque is obtained from the tendon forces by $\boldsymbol{\tau}_q = \boldsymbol{P}(\boldsymbol{q})\boldsymbol{f}_t$, where $\boldsymbol{P}^T = \frac{\partial \boldsymbol{h}(\boldsymbol{q})}{\partial \boldsymbol{q}}$ leading to

$$\boldsymbol{K}_q(\boldsymbol{q}) = \frac{\partial \boldsymbol{P}(\boldsymbol{q})^T}{\partial \boldsymbol{q}}\boldsymbol{f}_t + \boldsymbol{P}(\boldsymbol{q})^T \frac{\partial \boldsymbol{f}_t^T}{\partial \boldsymbol{q}} \boldsymbol{K}_q(\boldsymbol{q}) = \frac{\partial \boldsymbol{P}(\boldsymbol{q})^T}{\partial \boldsymbol{q}}\boldsymbol{f}_t + \boldsymbol{P}(\boldsymbol{q})^T \frac{\partial \boldsymbol{f}_t^T}{\partial \boldsymbol{h}} \frac{\partial \boldsymbol{h}^T}{\partial \boldsymbol{q}}. \tag{5.11}$$

By definition of the coupling matrix and defining $\boldsymbol{K}_t \in \mathbb{R}^{m \times m}$ ($\boldsymbol{K}_t(i,i) = k_{t_i}$, 0 otherwise, where $k_{t_i} \in \mathbb{R}^+, \forall i \in [0 \dots m-1]$ is the individual tendon stiffness), the stiffness transformation from tendon to link is

$$\boldsymbol{K}_q = \frac{\partial \boldsymbol{P}(\boldsymbol{q})^T}{\partial \boldsymbol{q}}\boldsymbol{f}_t + \boldsymbol{P}(\boldsymbol{q})^T \boldsymbol{K}_t \boldsymbol{P}(\boldsymbol{q}). \tag{5.12}$$

In a case of a position independent coupling matrix, i. e. constant pulley radii, the equation simplifies to

$$\boldsymbol{K}_q = \boldsymbol{P}^T \boldsymbol{K}_t \boldsymbol{P}. \tag{5.13}$$

Link side position

The joints of the fingers do not have a position sensor. On the one hand this provides a high robustness but on the other hand it implies that the link position must be estimated from the tendon displacements. As presented in the spring mechanism section, the change of length of tendon due to the spring mechanism is measured with the magnetic sensor. The displacement

of the tendon due to the motor is easily obtained with the motor position and the pulley radius. Therefore, the tendon displacement at the finger base is measured. The problem is mathematically formulated as

$$\min_{\boldsymbol{q}_x} \left(\sum_{i=1}^{8} \left(h_{xi}^{meas} - h_{xi}(\boldsymbol{q}) \right)^2 \right), \tag{5.14}$$

where $\boldsymbol{q}_x \in \mathbb{R}^4$ are the joint angles of finger x. h_{xi}, with $i \in [0 \dots 7]$, are the model-based lengths of the tendons and h_{xi}^{meas}, with $i \in [0 \dots 7]$, are the measured tendon lengths.

The solution $\boldsymbol{q}_x^* \in \mathbb{R}^n$ to the problem of eq.(5.14) is known to be obtained from the pseudo inverse of $\boldsymbol{P}_x \in \mathbb{R}^{n \times m}$,

$$\boldsymbol{q}_x^* = \boldsymbol{P}_x^+ \boldsymbol{h}^{meas} + \boldsymbol{q0}_x, \tag{5.15}$$

where $\boldsymbol{P}_x^+ = \boldsymbol{P}_x(\boldsymbol{P}_x \boldsymbol{P}_x^T)^{-1}$ is the Moore-Penrose pseudo inverse of the coupling matrix $\boldsymbol{P}_x$ of finger x. $\boldsymbol{h}_x^{meas} \in \mathbb{R}^m$ is the vector of the measured tendon lengths and $\boldsymbol{q0}_x \in \mathbb{R}^n$ is some arbitrary reference position of the joints. It is important to note that the pseudo inverse is always well defined since $\boldsymbol{P}_x$ is constant and matrix has full column rank.

5.3 Ring and fifth fingers

In this section, the specificity of the ring and fifth finger couplings are discussed. The kinematic and dynamic modeling only need minor modifications. Similarily, the tendon couplings need to be modified to account for the reduced count of tendons.

5.3.1 Kinematic model

The kinematic models are derived using homogeneous transformation matrices. The only required modification is to replace the joint angles q_{43} (resp. q_{53}) by its expression in terms of q_{42} (resp. q_{52}). The needed relationships, obtained from the pulley radii, are reported in Equation (5.17).

$$q_{43} = \frac{r_{43}}{r_{42}} q_{42} \tag{5.16}$$

$$q_{53} = \frac{r_{53}}{r_{52}} q_{52} \tag{5.17}$$

5.3.2 Dynamic model

In order to establish the dynamic equations, two methods are available. A first method consists in replacing the relationship of (5.17), the bone transformations, and the inertias in the dynamic model of the index finger.

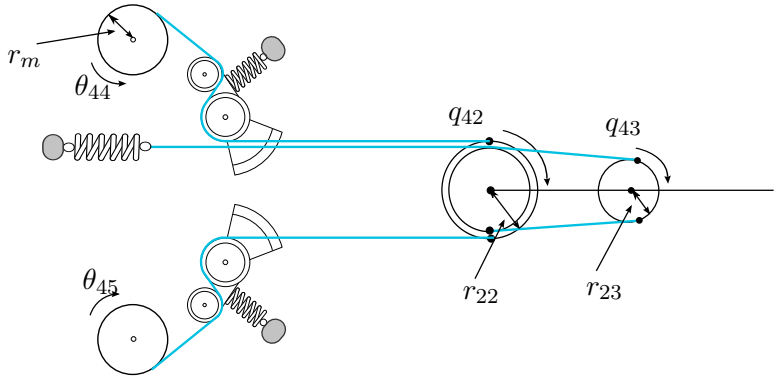

Figure 5.11: Mechanical realization of the PIP/DIP coupling of the ring and fifth fingers (case of the ring finger)

The second method consists in modifying the expression of the kinetic energy and the potential energy in the Lagrangian. Both methods are leading to the same results. However, the second method leads to a more efficient formulation of the dynamics.

5.3.3 Tendon coupling

As mentioned above, the ring and fifth fingers have a mechanical coupling between the PIP and DIP joints. In other words, the two joints are actuated by only 2 motors. Figure 5.11 depicts the mechanical realization of the underactuated joint. The coupling matrix $\boldsymbol{P}_4 \in \mathbb{R}^{6\times 3}$ is obtained by expressing the tendon lengths of the ring, $h_{4i}(\boldsymbol{q})$, with $i \in [0 \dots 5]$, and deriving them with respect to the joint positions $\boldsymbol{q}_{4i}$ ($i \in [0 \dots 3]$). According to the notations of Figure 5.11, the coupled tendon lengths are

$$\begin{array}{rcl} h_{44}(\boldsymbol{q}) & = & h0_{44} + r_{42}q_{42} \\ h_{45}(\boldsymbol{q}) & = & h0_{45} - r_{42}q_{42} \\ h_{46}(\boldsymbol{q}) & = & h0_{46} + (r_{42} + r_{43})q_{42} \\ h_{47}(\boldsymbol{q}) & = & h0_{47} - (r_{42} + r_{43})q_{42}, \end{array} \tag{5.18}$$

where $h0_{4i}$, with $i \in [0 \dots 7]$ denotes the initial (arbitrary reference) tendon length in the ring finger. $q_{4i} \in \mathbb{R}, i \in [0 \dots 3]$ are the joint angles. $r_{4j} \in \mathbb{R}$, with $j \in [1 \dots 5]$ are the pulley radii of the ring finger at joint j (the case of the fifth finger is obtained by replacing 4 by 5 in the previous expressions).

5.4 Thumb

According to numerous biomechanical authors [119–121] the hand would not be more than a spatula if it were not for the thumb. Anthropologists, like Kuczynski, have assumed that the thumb is what makes the human brain so

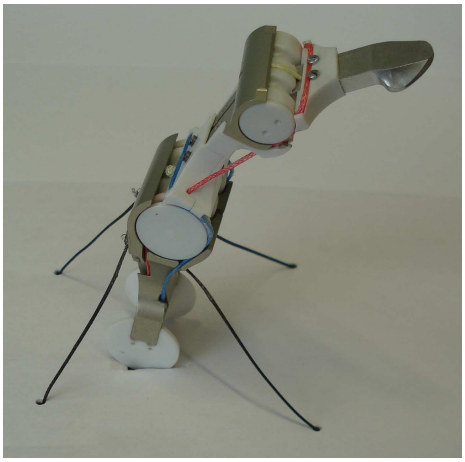

Figure 5.12: Thumb of the Hand Arm System

different from the monkeys. Intuitively, it is obvious that a poorly designed (or poorly controlled) thumb jeopardizes most of the hand functionality. Therefore, the modeling and control of the thumb of the Hand Arm System is one of the focus of this section.

The thumb has been carefully designed and several guidelines have been published in [122]. Very recent work also demonstrated the grasping capabilities of the hand [123]. The thumb PIP and DIP joints are similar to the other fingers but is using larger pulley radii to increase the maximum torques. The base, however, has a different structure. As depicted in Figure 5.12, the joint is driven by four tendons that are emerging from the palm and directly connected below the PIP joint. This structure, called a tensegrity structure, provides an increased maximum joint torque (through the increased moment arm).

The structure creates a nonlinear relationship between the base joint positions $(q_{11}, q_{12}) \in \mathbb{R}^2$ and the tendon lengths $h_{1i} \in \mathbb{R}, i \in [0 \dots 3]$.

5.4.1 Kinematic model

The kinematics of the thumb is computed from the homogeneous transformations of the joints and the bones. The difference with the index finger is that the partial transformation to the base of the PIP (${}^0_4\boldsymbol{T}_{thumb}$) will be used to compute the tendon coupling.

5.4.2 Dynamics model

The dynamical equations of the thumb are obtained from the kinematic equations and the inertia properties of each link. Since the inertia of the tendon is neglectable, there is no difference with the case of the index finger.

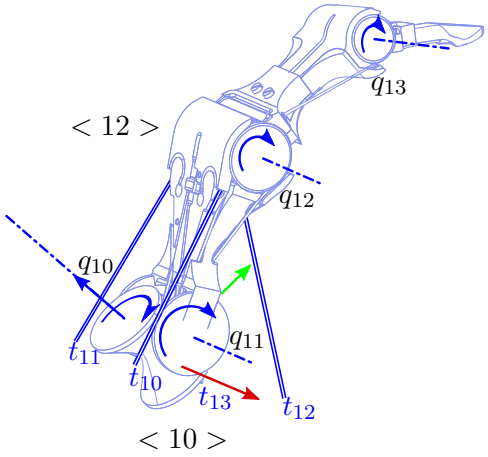

Figure 5.13: Joint axis and tendon names of the thumb of the Hand Arm System

5.4.3 Tendon coupling

Contrarily to the other fingers, the coupling of the thumb is nonlinear and position dependent.

The base joints (q_{10}, q_{11}) are driven by a set of four tendons that are directly inserted below the PIP joint (cf. Fig. 5.14). In order to express the lengths (or the change of lengths) of the base tendons, the coordinates of the tendon insertions points must be expressed in the same coordinate system. To this end the following steps are performed:

- the transformation from the thumb base coordinate system (cf. Fig. 5.13, frame $\{10\}$) to the coordinate system of the PIP base is extracted from the forward kinematics.

- the tendon insertion coordinates $[{}^{12}\boldsymbol{p}_{1i}, 1] \in \mathbb{R}^4, \quad i \in [0 \dots 3]$ (expressed in $\{12\}$) are transformed to the base frame $\{10\}$ with,

$$[{}^{10}\boldsymbol{p}_{1i}, 1] = {}^{12}_{10}\boldsymbol{T}[{}^{12}\boldsymbol{p}_{1i}, 1], \quad \forall i \in [0 \dots 3] \tag{5.19}$$

  where ${}^{12}_{10}\boldsymbol{T} \in \mathbb{R}^{4\times4}$ is the homogeneous transformation from $\{12\}$ to $\{10\}$.

The coordinates of the distal (resp. palmar) insertion of the tendons are more conveniently denoted A, B, C and D (resp. A_0, B_0, C_0 and D_0, cf. Fig. 5.14). The coordinates are reported in Table 5.2. The tendon lengths

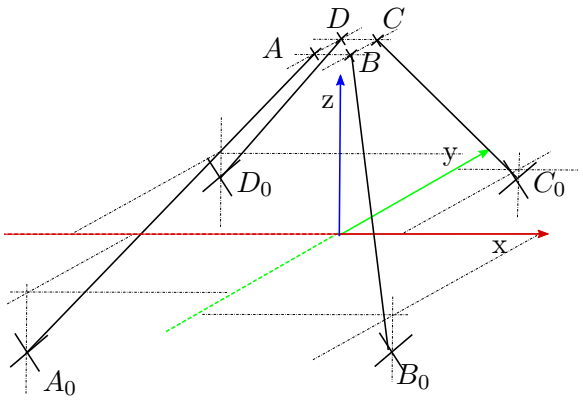

Figure 5.14: Thumb of the Hand arm system

Table 5.2: Coordinates of the bone insertion points for the tendons

Point	Coordinates [m]
A_0	$[0.002, 0.030, -0.025]$
B_0	$[0.002, 0.030, 0.025]$
C_0	$[0.002, -0.030, -0.025]$
D_0	$[0.002, -0.030, 0.025]$
A	$[0.002, 0.030, -0.025]$
B	$[0.002, 0.030, 0.025]$
C	$[0.002, -0.030, -0.025]$
D	$[0.002, -0.030, 0.025]$

$h_{1i}(\boldsymbol{q}) \in \mathbb{R}, \quad i \in [0 \dots 3]$ of the thumb base are obtained as

$$\begin{aligned} h_{thumb,0} &= |A(q_{10}, q_{11}) - A_0| \\ h_{thumb,1} &= |B(q_{10}, q_{11}) - B_0| \\ h_{thumb,2} &= |C(q_{10}, q_{11}) - C_0| \\ h_{thumb,3} &= |D(q_{10}, q_{11}) - D_0|. \end{aligned} \tag{5.20}$$

The PIP and DIP tendons are going through the base and rolling on the PIP and DIP joints. Therefore, their length is linearly dependent on the finger position.

Applied to the thumb finger, the coupling matrix has a block diagonal shape (cf. Fig. 5.15). The lower right part (i. e. the PIP and DIP couplings) is

$$\boldsymbol{P}_{thumb}([3:4],[5:8]) = \begin{bmatrix} -r_{12} & 0 \\ r_{12} & 0 \\ r_{12} & -r_{13} \\ -r_{12} & r_{13} \end{bmatrix}, \tag{5.21}$$

The submatrix selection is following MATLAB®convention[2]. The complete tendon lengths are

$$\begin{aligned} h_{thumb,0} &= h0_{thumb,0} + |A(q_{10}, q_{11}) - A_0| \\ h_{thumb,1} &= h0_{thumb,1} + |B(q_{10}, q_{11}) - B_0| \\ h_{thumb,2} &= h0_{thumb,2} + |C(q_{10}, q_{11}) - C_0| \\ h_{thumb,3} &= h0_{thumb,3} + |D(q_{10}, q_{11}) - D_0| \\ h_{thumb,4} &= h0_{thumb,4} + r_{12}q_{12} \\ h_{thumb,5} &= h0_{thumb,5} - r_{12}q_{12} \\ h_{thumb,6} &= h0_{thumb,6} - r_{12}q_{12} + r_{13}q_{13} \\ h_{thumb,7} &= h0_{thumb,7} + r_{12}q_{12} - r_{13}q_{13}. \end{aligned} \tag{5.22}$$

where $h0_{thumb,i}$ with $i \in [0..7]$ is the initial tendon length when the finger is at its reference position (i. e. $\boldsymbol{q} = \boldsymbol{q0}$), (r_{12}, r_{13}) are the radii of the joint pulleys. The coupling matrix $\boldsymbol{P}_{thumb} \in \mathbb{R}^{4\times 8}$ is obtained by taking the partial derivative of the tendon length $h_{thumb,i}$ with $i \in [0..7]$ w. r. t. the joint position q_{1j} with $j \in [0..3]$.

Stiffness transformation

The equation for the stiffness transformation from tendon stiffness to joint stiffness is identical to the ones of the index finger. However, since the

[2]Indexing is one based, in (5.21) the selection consists of the two last columns and the four last lines

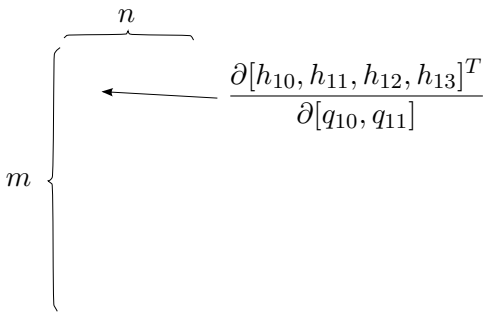

Figure 5.15: Structure of the coupling matrix

coupling matrix is depending on the base position, the generic form must be used,

$$\boldsymbol{K}_q = \frac{\partial \boldsymbol{P}(\boldsymbol{q})^T}{\partial \boldsymbol{q}} \boldsymbol{f} + \boldsymbol{P}(\boldsymbol{q})^T \boldsymbol{K}_t \boldsymbol{P}(\boldsymbol{q}), \tag{5.23}$$

where $q \in \mathbb{R}^n$ is the vector of joint position. $\boldsymbol{K}_q \in \mathbb{R}^{n \times n}$ (resp. $\boldsymbol{K}_t \in \mathbb{R}^{m \times m}$) is the joint stiffness matrix (resp. the diagonal stiffness matrix of the tendons). $\boldsymbol{P}(\boldsymbol{q}) \in \mathbb{R}^{m \times n}$ is the position dependent coupling matrix. $\boldsymbol{f} \in \mathbb{R}^m$ is the vector of tendon forces.

Link position estimation

As in the case of the fingers, the thumb does not have a position sensor. But the pseudo inversion that was used for the linear couplings can not be used for the thumb. Indeed, the coupling matrix is position dependent and the solution to the least square problem is not anymore a simple pseudo inversion. The problem is mathematically formulated as

$$\min_{\boldsymbol{q}} \left(\sum_{i=1}^{7} \left(\hat{h}_{1i} - h_{1i}(\boldsymbol{q}) \right)^2 \right), \tag{5.24}$$

where $q_{1i} \in \mathbb{R}$ with $i \in [0 \dots 3]$ are the base joint angles, h_{1i} with $i \in [0 \dots 7]$ (resp. $\hat{h}_{1i}$) are the analytic length of the tendon i of the thumb (resp. the measured tendon lengths). However, the structure of the thumb implies that only the four base tendons are involved in the nonlinear, position dependant coupling. Therefore, the link side position estimation for the PIP and DIP joints of the thumb are similar to the one of the index finger.

The position estimation for the base must be realized online and therefore has been implemented as a fixed step gradient search. The algorithm is reported in the pseudo code Algorithm 1.

In order to evaluate the algorithm, a grid of tendon position vectors is generated from the kinematic model. The algorithm is evaluated on this vector grid and the resulting joint positions are compared to the ground

Algorithm 1 Pseudo Code of the gradient search algorithm use to estimate the link side position

$B \Leftarrow \ker P$
$\alpha \Leftarrow \alpha_0$
$grad \Leftarrow grad_0$
$step \Leftarrow step_0$
$C_{best} \Leftarrow +\inf$
for $i = 1$ to 50 **do**
  $C, grad \Leftarrow cost_\alpha(\alpha - grad.step)$
  if $C < C_{best}$ **then**
    $\alpha \Leftarrow \alpha - grad.step$
  else
    $step \Leftarrow \frac{step}{2}$
  end if
end for

truth. Fig. 5.16 depicts the results obtained with 30 steps. The two axes are representing the joint angles for the flexion/extension q_{10} and abduction/adduction q_{11} motions. The red circles are the original points and the blue crosses are the estimated coordinates.

In order to check the robustness for the real implementation, a set of vectors with a noise (the amplitude of the noise was 0 [mm], 0.5[mm] and 1[mm]) to simulate the measurement inaccuracy is evaluated. The number of steps is also modified in order to select the optimal value for the real time code. Unlike the implemented code, the search is always started from $(q_{10}, q_{11}) = [0, 0]$, which explains the incorrect results far from the origin. The results are reported in Fig. 5.17. The required number of iterations is easily achieved in real time. Moreover when using the previous solution as a starting point the search always reaches the minimum step size after only a few iterations.

5.5 Hematometacarpal joint

Because the design of a robotic hand is challenging, most of the designs are not spending as much effort in designing the fifth finger as for the other fingers. In the hand of the Hand Arm System the fifth finger base joint received a particular attention. The hematometacarpal joint, i. e. the joint between the fifth finger metacarpal and the palm, has been designed as a four bars linkage mechanism. This allows to mimic the human metacarpal motion and especially provides a locking motion towards the palm center when the joint limits are reached.

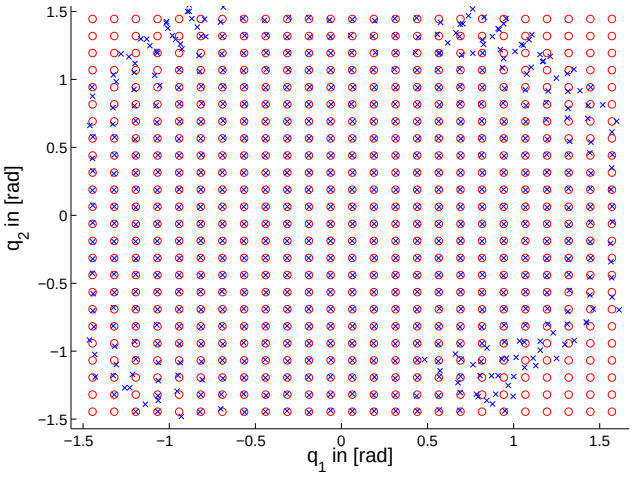

Figure 5.16: Link position estimation : gradient search results with 30 iterations. The red circles are the original points and the blue crosses are the estimated coordinates. The search was always started from (0,0) which explains the errors in the corners. In practice the last value is used as a starting point.

5.6 Conclusion

This chapter presented the modeling of the fingers. The kinematics are obtained from the bone transformations and homogenous transformations. The dynamics are obtained from the systematic Newton-Euler method. The tendon path through the forearm, the wrist, the palm and the fingers is used to derived the coupling matrices. The coupling matrices are further used to estimate the joint positions. However, the special actuation of the thumb by a tensegrity structure creates a nonlinear problem that has been solved with a realtime projected gradient algoritm.

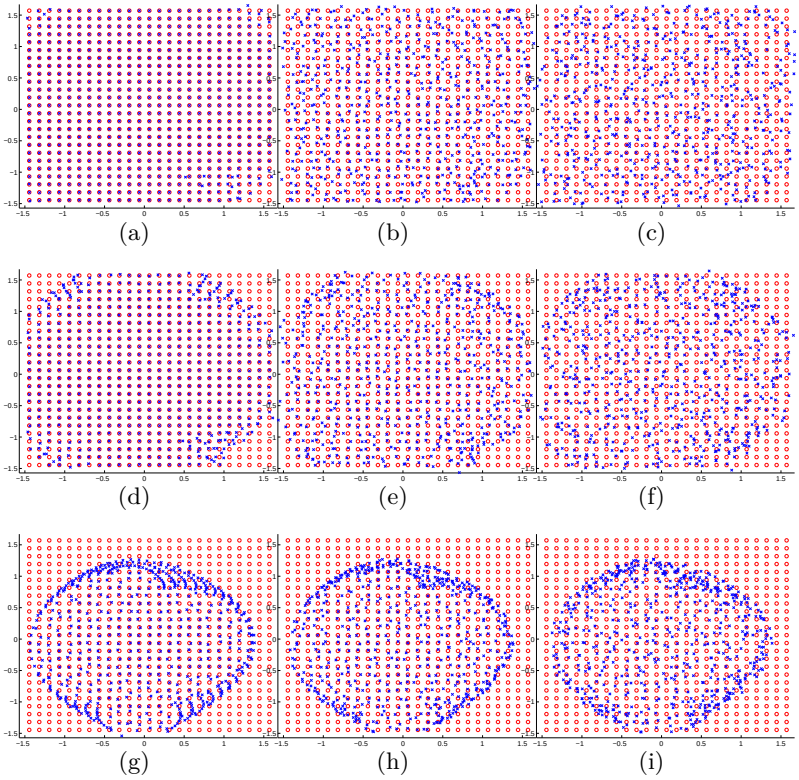

Figure 5.17: Results of the link position estimation with different step size and step count. In each plot, the x and y axis are representing the base joint angle q_{10} and q_{11}. The red circles denote the coordinates used for generation of the tendon length set. The blue crosses depict the result. Ideally, the crosses and circles should match. 5.17a : 50 iterations, 0mm noise. 5.17b : 50 iterations, 0.5mm noise. 5.17c : 50 iterations, 1mm noise. 5.17a : 30 iterations, 0mm noise. 5.17b : 30 iterations, 0.5mm noise. 5.17c : 30 iterations, 1mm noise. 5.17a : 15 iterations, 0mm noise. 5.17b : 15 iterations, 0.5mm noise. 5.17c : 15 iterations, 1mm noise.

6 Wrist Model

The arm and the hand are connected with a wrist, which is actuated with an helping antagonistic concept [2]. Since the motors are located in the forearm all the tendons are guided from the motors to the fingers through the wrist. Therefore, the wrist must withstand the combined load of all the tendons and has been designed to support up to $8000N$ (the weight of a small car). Desirably, all the tendons would go through a unique point and no coupling would be introduced by the wrist motion. However, it is mechanically not possible to let 38 tendons cross at a unique point in space (the tendon would be damaged by the contact to other tendons). Consequently, the wrist is using two layers of 19 tendons that are spaced along the width of the wrist (see Fig. 6.1). Since the wrist can bend along two directions, each tendon should be guided by two pullies in each side of the wrist. The required total of 76 pulleys as well as the space required for their mounting did not allow for this optimal solution (in terms of friction and guiding). The selected solution guides the tendons only along the flexion extension axis of the wrist. The missing lateral guiding is ensured by the flanges of the pulleys and some mechanical grid that ensures that the tendons are not jumping to a different tendon path. Although the solution is suboptimal in terms of tendon guiding, it provides a compact wrist. Moreover, when limited to small abduction/adduction angles (which is the normal case), no significant friction is added. The tendons are not going through the center of rotation of the wrist (which is, as established below, moving over time), thus a motion of the wrist, if not compensated by the controller, creates a motion of the fingers. The change of length of tendon in the wrist must be calculated to have the possibility to compensate this effect using, for example, a feedforward term.

6.1 Kinematic model

This section concentrates on the kinematic modeling of the wrist. The method is explained step by step to tackle the overall complexity of the calculations. The wrist structure can be seen as a double inverted parallelogram. The frames and the angle labels relevant for the model are depicted in Fig. 6.2 and Fig. 6.3. The numerical values and symbols used for the wrist modeling are reported in Table 6.1.

The method can be decomposed as follows:

- Solving a single parallelogram problem in a plane defined by the wrist flexion/adduction axis (calculating t_C).
- Creating a temporary frame.

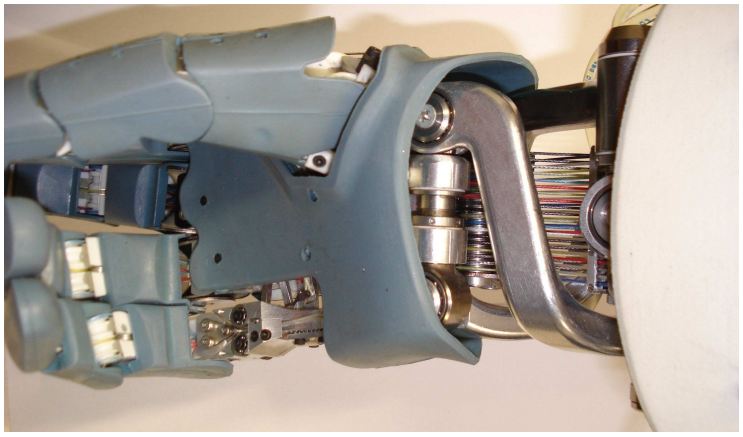

Figure 6.1: Wrist of the hand arm system. The two groups of 19 tendons are going through the wrist

Table 6.1: Wrist symbol definitions, units and values

Symbol	Description	Unit	Value
a	wrist length	$[m]$	0.050
b	wrist width	$[m]$	0.042
c	wrist thickness	$[m]$	0.036

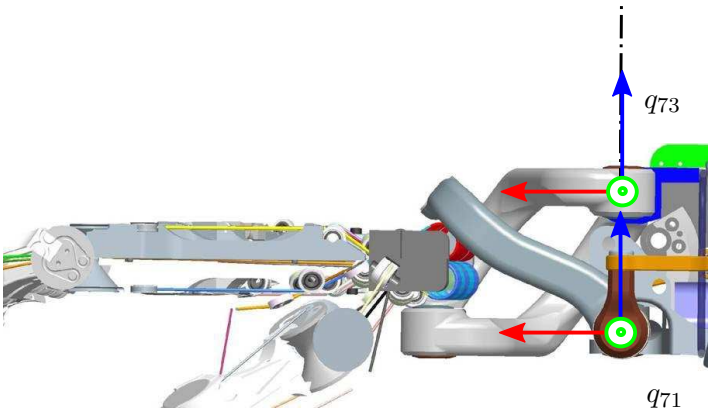

Figure 6.2: Side view of the wrist (CAD)

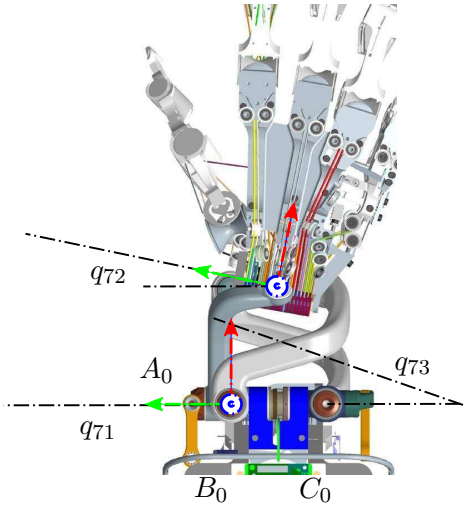

Figure 6.3: Top view of the wrist (CAD)

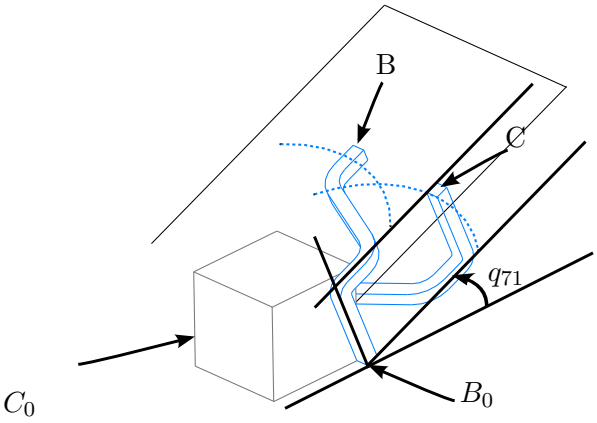

Figure 6.4: BC plane transformation (CAD)

- Expressing the distance constraint between two points in the coordinate system of the temporary frame (The point $\boldsymbol{A}$ in the palm and $\boldsymbol{A}_0$ in the forearm).
- Solving the distance constraint and transforming the coordinates of the solution into the forearm frame $\{0\}$.
- Building a frame $\{ABC\}$ from the coordinates of the 3 points of the palm $(\boldsymbol{A}, \boldsymbol{B}, \boldsymbol{C})$.

6.1.1 Calculation of angle t_C

The first step consists in solving the parallelogram problem defined in the upper plane of the wrist (cf. Fig. 6.4). As depicted in Fig. 6.5, the

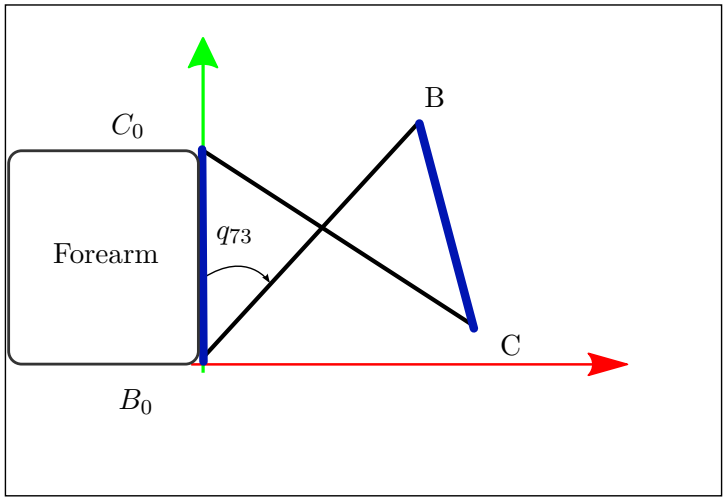

Figure 6.5: Distance constraints between $\boldsymbol{B}$ and $\boldsymbol{C}$ in the plane

coordinates of $\boldsymbol{B}$ and $\boldsymbol{C}$ can be expressed as

$$\boldsymbol{B} : \begin{cases} R_{BB_0} cos(t_B) \\ R_{BB_0} sin(t_B) \end{cases} \quad \text{and} \quad \boldsymbol{C} : \begin{cases} R_{CC_0} cos(t_C) \\ R_{CC_0} sin(t_C) \end{cases} \tag{6.1}$$

where $t_B = \frac{\Pi}{2} - q_{73}$ is the measure of the internal wrist angle obtained with a potentiometer. $t_C \in \mathbb{R}$ (resp. $t_B \in \mathbb{R}$) is an arbitrary parametrization of the circle of center $\boldsymbol{C}$ (resp. $\boldsymbol{B}$), $R_{BB_0} \in \mathbb{R}$ (resp. $R_{CC_0} \in \mathbb{R}$) is the radius of the circle of center $\boldsymbol{B}$ (resp. of center $\boldsymbol{C}$). But $\boldsymbol{B}$ and $\boldsymbol{C}$ are rigidly linked at a constant distance $D_{BC} \in \mathbb{R}$. Mathematically, the constraint on the length BC is:

$$\|BC\|^2 = (R_{BB_0} sin(q_3) - R_{CC_0} cos(t_C))^2 + (R_{BB_0} cos(q_3) - R_{CC_0} sin(t_C))^2 = D_{BC}^2. \tag{6.2}$$

Solving eq. (6.2) for q_3 gives two solutions,

$$\begin{aligned} t_C &= \arctan(\sin(t_B), \cos(t_B)), \\ t_C &= \arctan\left(\frac{(BC^2 + BB_0^2)\sin(t_B) - 2BB_0BC}{(BB_0^2 - BC^2)\cos(t_B)}\right). \end{aligned} \tag{6.3}$$

The first solution is the symmetric from $\boldsymbol{B}$ and therefore should be discarded. The second solution, once injected in the Equation of C (eq. (6.1)), yields

$$\boldsymbol{C} : \begin{cases} \dfrac{BB_0(BB_0^2 - BC^2)cos(t_B)}{-2BB_0BC\sin(t_B) + BC^2 + BB_0^2} \\ \dfrac{(BB_0^2 - BC^2)(BB_0 sin(t_B) - BC)}{-2BB_0BC\sin(t_B) + BC^2 + BB_0^2} \end{cases}. \tag{6.4}$$

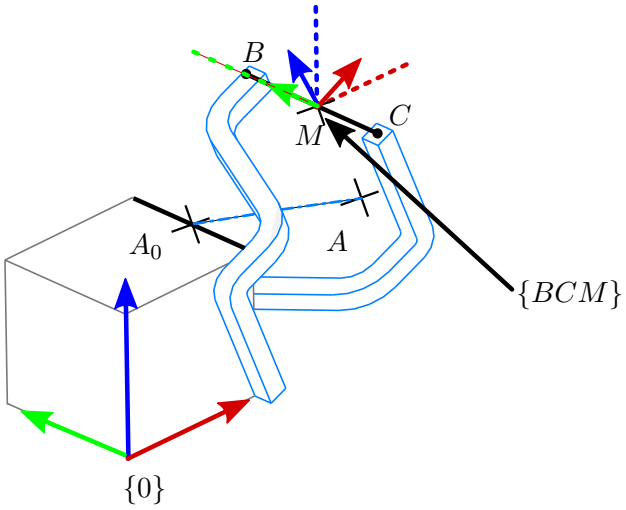

Figure 6.6: BC plane transformation with $\alpha = 0$ (CAD). A is located on a circle defined by $\|AB\| = \|AC\|$

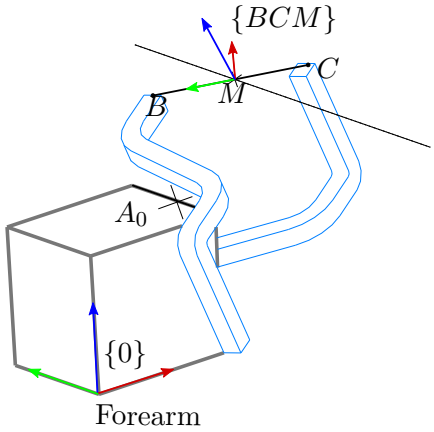

Figure 6.7: BC plane transformation with $\alpha = 30\,\text{deg}$ (CAD)

6.1.2 Calculation of angle t_A

The coordinates of the points $\boldsymbol{B}$ and $\boldsymbol{C}$ are known in the world coordinate system. Three distances constraints are left in order to determine the position of the last point of the palm $\boldsymbol{A}$: $\|AA_0\|$, $\|AB\|$, $\|AC\|$. However, a direct attempt to express and solve the constraints with a symbolic calculation tool failed. As depicted in Fig. 6.7 a coordinate system $\{BCM\}$ can be constructed. $\boldsymbol{M}$ is the middle of BC. $\boldsymbol{x}$ is aligned with MC, $\boldsymbol{z}$ is normal to the plane rotated around $\boldsymbol{x}$ (the original wrist frame) by an amount of q_{71}. $\boldsymbol{y} = \boldsymbol{z} \times \boldsymbol{x}$ simply completes the frame. It is interesting to remark that the distance constraints $\|AB\|$ and $\|AC\|$ are geometrically equivalent to saying that $\boldsymbol{A}$ is located on a circle (cf. Fig. 6.6, non degenerated intersection of two spheres), centered in M and in the plane orthogonal to BC containing $\boldsymbol{M}$ (because $\|AB\| = \|AC\|$). Based on this interpretation, the coordinates of $\boldsymbol{A}$ in $\{BCM\}$ have the simple form:

$$ {}^{BCM}\boldsymbol{A} : \begin{cases} x = 0 \\ y = R_{AA_0} cos(t_A) \\ z = R_{AA_0} sin(t_A) \end{cases} \tag{6.5} $$

The coordinates of $\boldsymbol{A}_0$ (in the coordinate system $\{BCM\}$), ${}^{BCM}\boldsymbol{A}_0$ are obtained with the transformation:

$$ [{}^{BCM}\boldsymbol{A}_0, 1] = {}^{BCM}_{0}\boldsymbol{T}[{}^{0}\boldsymbol{A}_0, 1] \tag{6.6} $$

where ${}^{0}\boldsymbol{A}_0$ (resp. ${}^{BCM}\boldsymbol{A}_0$) are the coordinates of A_0 in the frame $\{0\}$ (resp. $\{BCM\}$) and ${}^{BCM}_{0}\boldsymbol{T}$ is the homogeneous transformation matrix from the coordinate system $\{0\}$ to the coordinate system $\{BCM\}$.

$$ (A_{0x})^2 + (A_{0y} - R_{AA_0} cos(t_A))^2 + (A_{0z} - R_{AA_0} sin(t_A))^2 = d^2_{AA_0} \tag{6.7} $$

It remains to solve a distance constraint equation given by Eq. (6.7)) between $\boldsymbol{A}_0$ and A, both expressed in $< BCM >$. The equation is solved for t_A and re-injected in the coordinates of $\boldsymbol{A}$. The coordinates of A in $\{BCM\}$ are transformed back into $\{0\}$ with Eq. (6.8).

$$ [{}^{0}\boldsymbol{A}, 1] = {}_{BCM}{}^{0}\boldsymbol{T}[{}^{BCM}\boldsymbol{A}, 1] \tag{6.8} $$

where ${}^{0}\boldsymbol{A}$ (resp. ${}^{BCM}\boldsymbol{A}$) are the coordinates of A in the frame $\{0\}$ (resp. $\{BCM\}$) and ${}_{BCM}{}^{0}\boldsymbol{T}$ is the homogeneous transformation matrix from the coordinate system $\{BCM\}$ to the coordinate system $\{0\}$.

Finally, $\boldsymbol{A}$, $\boldsymbol{B}$ and $\boldsymbol{C}$ are used to build the palm base frame $\{ABC\}$, as depicted in Fig. 6.8. The lengths of the different tendons through the wrist are easily expressed from the frames $\{ABC\}$ and $\{A_0B_0C_0\}$.

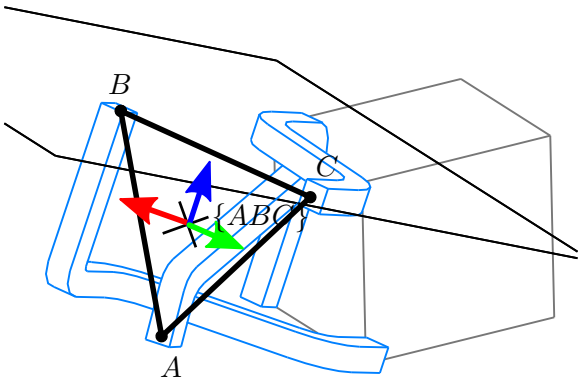

Figure 6.8: Palm frame ABC

Each tendon i with $i \in [1 \dots 38]$ is going through a fixed point in the palm ${}^{ABC}h_{palm,offset,i} \in \mathbb{R}^3$ and a fixed point in the forearm ${}^{0}h_{forearm,offset,i} \in \mathbb{R}^3$. Expressing the coordinates of the palm point ${}^{ABC}h_{palm,offset,i} \in \mathbb{R}^3$ in the forearm coordinate system $\{0\}$ allows to express the tendon lengths in the wrist

$$h_{wrist,i} = \left\| [{}^{0}h_{forearm,offset,i}, 1] - {}^{0}_{ABC}T[{}^{ABC}h_{palm,offset,i}, 1] \right\|, \qquad (6.9)$$

where ${}^{0}h_{forearm,offset,i}, i \in [1 \dots 38]$ and ${}^{ABC}h_{palm,offset,i}, i \in [1 \dots 38]$ are defined in the Table 6.2. As usual, the form $[x, y, z, 1]$ is used to perform homogeneous operations.

6.2 Kinematic verification

A first simulation consists in a flexion/extension motion of 30 degrees followed by an abduction/adduction of 20 degrees. It allows to verify that the modeling of the wrist kinematics and the tendon coupling is globally correct. Figure 6.9 shows that the errors in the constraints are limited to numerical inaccuracies.

The tendon displacements resulting from the wrist motion are depicted in Figure 6.10 and give an insight in the way the wrist interacts with the fingers. According to the designer of the wrist, the coupling with the finger during the flexion/extension should be minimal. This is confirmed by the first part of the plot where the motion is only performed in the flexion/extension direction. Moreover, the shape of the elongation confirms that the coupling is nonlinearly related to the wrist flexion angle. The abduction/adduction motion has a large influence on the tendon lengths. The perturbation is directly proportional to the distance to the median axis of the wrist (i. e. the tendons in the center of the wrist are barely moving while the side ones are undergoing the largest motions). Similar to the flexion/extension

Table 6.2: Tendon offset in the forearm frame and in the palm frame

Tendon	Forearm	Palm
1	[0.004, 0.007, 0.008]	[-0.004, -0.011, 0.010]
2	[0.004, 0.008, 0.008]	[-0.004, -0.010, 0.010]
3	[0.004, 0.010, 0.008]	[-0.004, -0.008, 0.010]
4	[0.004, 0.011, 0.008]	[-0.004, -0.006, 0.010]
5	[0.004, 0.013, 0.008]	[-0.004, -0.005, 0.010]
6	[0.004, 0.015, 0.008]	[-0.004, -0.003, 0.010]
7	[0.004, 0.016, 0.008]	[-0.004, -0.002, 0.010]
8	[0.004, 0.018, 0.008]	[-0.004, 0.000, 0.010]
9	[0.004, 0.019, 0.008]	[-0.004, 0.002, 0.010]
10	[0.004, 0.021, 0.008]	[-0.004, 0.003, 0.010]
11	[0.004, 0.023, 0.008]	[-0.004, 0.005, 0.010]
12	[0.004, 0.024, 0.008]	[-0.004, 0.006, 0.010]
13	[0.004, 0.026, 0.008]	[-0.004, 0.008, 0.010]
14	[0.004, 0.027, 0.008]	[-0.004, 0.010, 0.010]
15	[0.004, 0.029, 0.008]	[-0.004, 0.011, 0.010]
16	[0.004, 0.031, 0.008]	[-0.004, 0.013, 0.010]
17	[0.004, 0.032, 0.008]	[-0.004, 0.014, 0.010]
18	[0.004, 0.034, 0.008]	[-0.004, 0.016, 0.010]
19	[0.004, 0.035, 0.008]	[-0.004, 0.018, 0.010]
20	[0.004, 0.006, 0.028]	[-0.004, -0.013, -0.010]
21	[0.004, 0.007, 0.028]	[-0.004, -0.011, -0.010]
22	[0.004, 0.009, 0.028]	[-0.004, -0.010, -0.010]
23	[0.004, 0.011, 0.028]	[-0.004, -0.008, -0.010]
24	[0.004, 0.012, 0.028]	[-0.004, -0.006, -0.010]
25	[0.004, 0.014, 0.028]	[-0.004, -0.005, -0.010]
26	[0.004, 0.015, 0.028]	[-0.004, -0.003, -0.010]
27	[0.004, 0.017, 0.028]	[-0.004, -0.002, -0.010]
28	[0.004, 0.019, 0.028]	[-0.004, 0.000, -0.010]
29	[0.004, 0.020, 0.028]	[-0.004, 0.002, -0.010]
30	[0.004, 0.022, 0.028]	[-0.004, 0.003, -0.010]
31	[0.004, 0.023, 0.028]	[-0.004, 0.005, -0.010]
32	[0.004, 0.025, 0.028]	[-0.004, 0.006, -0.010]
33	[0.004, 0.027, 0.028]	[-0.004, 0.008, -0.010]
34	[0.004, 0.028, 0.028]	[-0.004, 0.010, -0.010]
35	[0.004, 0.030, 0.028]	[-0.004, 0.011, -0.010]
36	[0.004, 0.031, 0.028]	[-0.004, 0.013, -0.010]
37	[0.004, 0.033, 0.028]	[-0.004, 0.014, -0.010]
38	[0.004, 0.035, 0.028]	[-0.004, 0.016, -0.010]

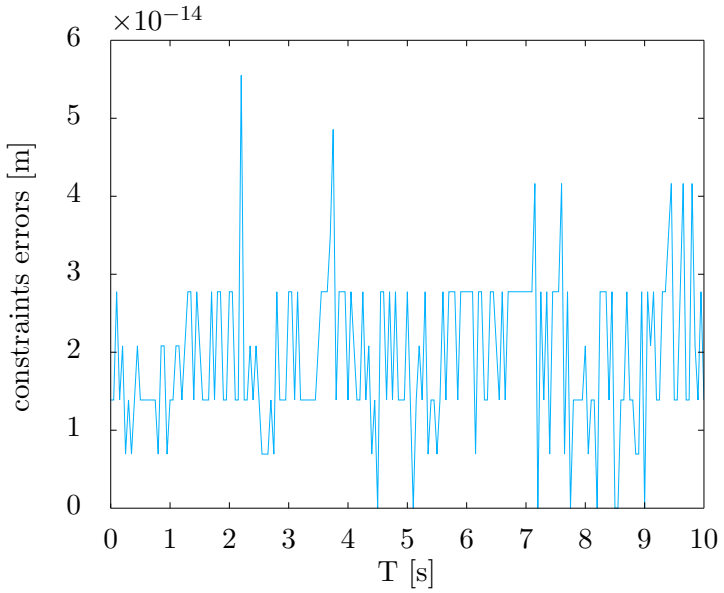

Figure 6.9: Simulation: maximum error on the distance constraints between the points, that is $\max(\|AA_0\|, \|BB_0\|, \|CC_0\|, \|AB\|, \|AC\|, \|BC\|)$

case, the relationship between the displacements and the input angle are nonlinear.

During the experiments, the tendons are controlled by a force controller such that the motors are simply following the tendon displacement imposed by the wrist coupling. Figure 6.11 shows how the tendons are moving according to the imposed wrist motion.

To verify more precisely the model, a simulation and the corresponding experiment are compared in order to verify that the wrist frame calculation and the tendon length calculations are correct. In the experiments, the wrist is driven manually while the fingers are fixed to a reference plate. Figure 6.10 reports the calculated tendon displacement due to the wrist motion. Figure 6.12 (resp. Figure 6.13) reports the measured tendon displacement due to the wrist abduction/adduction (resp. flexion/extension) motion. The identical patterns indicate that the modeled lengths are matching the real tendon displacements.

The discrepancies between the plots can be explained by the steady-state error of the tendon force controller added to the approximated contact model between the tendon and the pulleys (they are considered fixed points in the wrist although the contact points are changing slightly due to the approach angle).

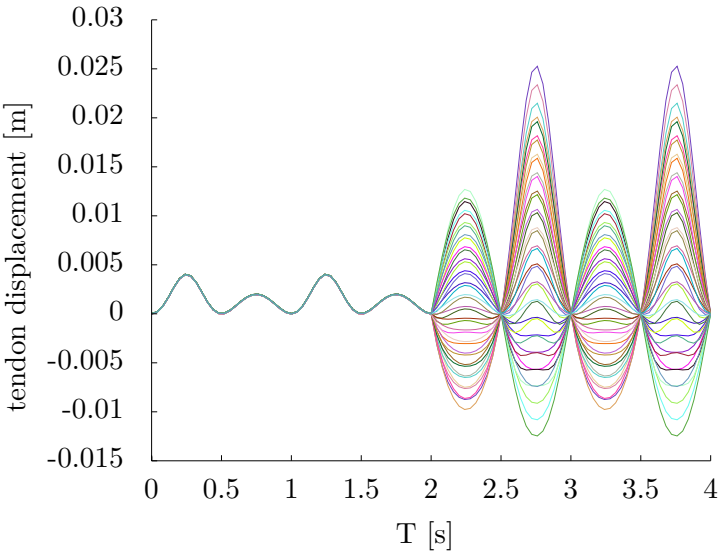

Figure 6.10: Simulation: calculated tendon displacement resulting from a wrist motion

6.3 Conclusion

The wrist has a double inverted parallelogram structure. This allows all tendons to be guided through the wrist while providing a large range of motion. However, because the tendons cannot all go through a unique point, a motion of the wrist modifies the tendon path which results in a motion in the fingers. Forwarding the tendon length of the wrist prevents the finger position deviations. Therefore, the homogeneous transformation between the forearm frame and the palm frame has been derived. It should be noted that the wrist position modifies the mechanical stiffness of the tendons since the wrist is also actuated with a stiffness-adjustable mechanism. The exact expression of the mechanical stiffness of the fingers, including the wrist contribution, is however not treated in this thesis. Simulations and experiments confirm the behavior announced by the designers. The good match between the simulated and the measured the tendon displacements validate the wrist kinematic model.

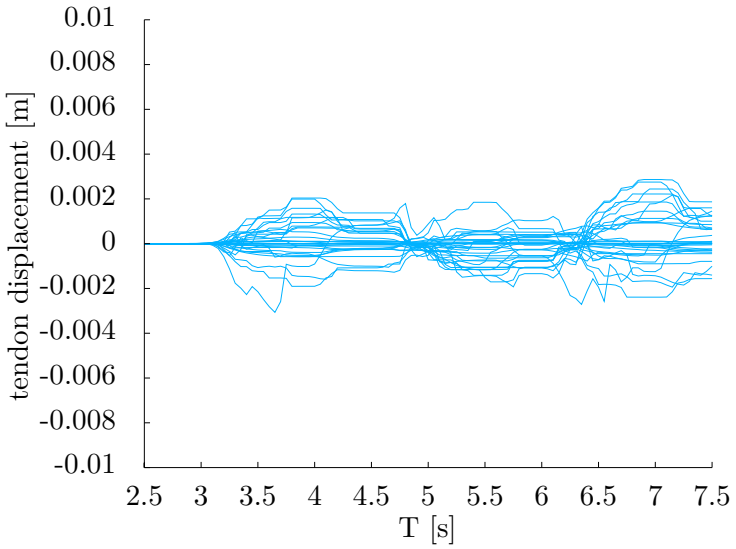

Figure 6.11: Experiment: measured tendon displacement resulting from the recorded wrist motion

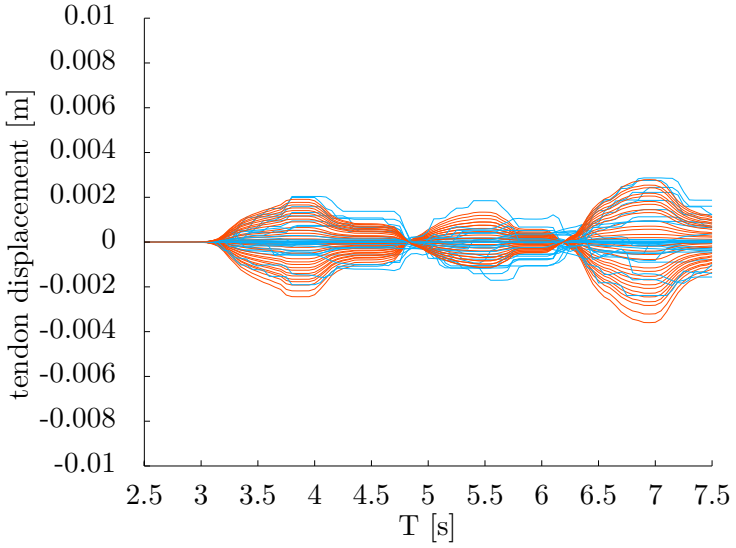

Figure 6.12: Experiment: simulated tendon displacement resulting from the recorded wrist flexion/extension motion

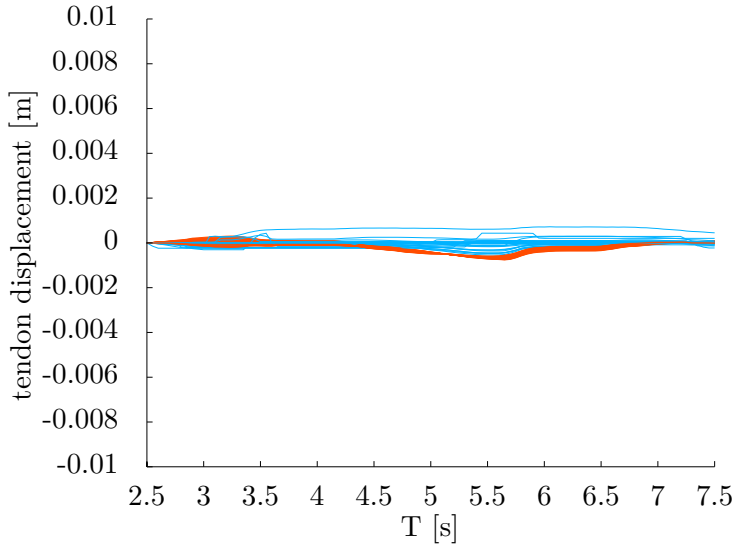

Figure 6.13: Experiment: measured tendon displacement resulting from the recorded wrist abduction/adduction